

**CAMELE: Collocation-Analyzed Multi-source Ensembled Land
Evapotranspiration Data**

Changming Li¹, Ziwei Liu¹, Wencong Yang¹, Zhuoyi Tu¹, Juntai Han¹, Sien Li²,
Hanbo Yang^{1*}

¹State Key Laboratory of Hydrosience and Engineering, Department of Hydraulic
Engineering, Tsinghua University. Beijing 100084, China

²Center for Agricultural Water Research in China, China Agricultural University,
Beijing 100083, China

*Correspondence: Hanbo Yang (yanghanbo@tsinghua.edu.cn)

Abstract

Land evapotranspiration (ET) plays a crucial role in Earth's water-carbon cycle, and accurately estimating global land ET is vital for advancing our understanding of land-atmosphere interactions. Despite the development of numerous ET products in recent decades, widely used products still possess inherent uncertainties arising from using different forcing inputs and imperfect model parameterizations. Furthermore, the lack of sufficient global in-situ observations makes direct evaluation of ET products impractical, impeding their utilization and assimilation. Therefore, establishing a reliable global benchmark dataset and exploring evaluation methodologies for ET products is paramount. This study aims to address these challenges by (1) proposing a collocation-based method that considers non-zero error cross-correlation for merging multi-source data and (2) employing this merging method to generate a long-term daily global ET product at resolutions of 0.1° (2000-2020) and 0.25° (1980-2022), incorporating inputs from ERA5L, FluxCom, PMLv2, GLDAS, and GLEAM. The resulting product is the Collocation-Analyzed Multi-source Ensembled Land Evapotranspiration Data (CAMELE). CAMELE exhibits promising performance across various vegetation coverage types, as validated against in-situ observations. The evaluation process yielded Pearson correlation coefficients (R) of 0.63 and 0.65, root-mean-square-errors (RMSE) of 0.81 and 0.73 mm/d, unbiased root-mean-square-errors (ubRMSE) of 1.20 and 1.04 mm/d, mean absolute errors (MAE) of 0.81 and 0.73 mm/d, and Kling-Gupta efficiency (KGE) of 0.60 and 0.65 on average over resolutions of 0.1° and 0.25° , respectively. In addition, comparisons indicate that CAMELE can effectively characterize the multi-year linear trend, mean average, and extreme values of ET. However, it exhibits a tendency to overestimate seasonality. In summary, we propose a reliable set of ET data that can aid in understanding the variations in the water cycle and has the potential to serve as a benchmark for various applications.

1. Introduction

Land evapotranspiration (ET) plays a critical role in the global water and energy cycles, encompassing various processes such as soil evaporation, vegetation transpiration, canopy interception, and surface water evaporation (Zhang et al., 2019; Zhao et al., 2022; Lian et al., 2018). Accurately estimating global land evapotranspiration is vital for understanding the hydrological cycle and land-atmosphere interactions, as it serves as an intermediary variable connecting soil moisture, air temperature and humidity (Miralles et al., 2019; Gentile et al., 2019). Therefore, providing a reliable ET dataset as a benchmark for further research is crucial.

In recent decades, numerous studies have focused on estimating global land evapotranspiration, resulting in many datasets (Yang et al., 2023). However, discrepancies often arise among these simulations due to algorithm and principle variations (Restrepo-Coupe et al., 2021; Han and Tian, 2020). Additionally, evaluating ET products is challenging due to the limited availability of global-scale observations, which hampers their direct use (Pan et al., 2020; Baker et al., 2021).

The fusion of multi-source data is a suitable option to address these uncertainties. Recent studies have explored several approaches to integrate multiple ET products, including Simple Average (SA) (Ershadi et al., 2014), Bayesian Model Average (BMA) (Hao et al., 2019; Ma et al., 2020; Zhu et al., 2016), Reliability Ensemble Average (REA) (Lu et al., 2021), Empirical Orthogonal Functions (EOF) (Feng et al., 2016) and machine-learning-based methods (Chen et al., 2020; Yin et al., 2021). However, the primary challenge lies in calculating reliable input weights based on a selected "truth" (Koster et al., 2021), which can involve averaging or incorporating other relevant geographical information as a benchmark.

Recently, collocation methods have emerged as promising techniques for estimating random error variances and data-truth correlations in collocated inputs (Stoffelen, 1998; Li et al., 2022, 2023c; Park et al., 2023). These methods consider the errors

68 associated with collocated datasets as an accurate representation of uncertainty
 69 without assuming the absence of errors in any datasets. It is important to note that
 70 while collocation methods, such as the triple collocation (TC) and the extended
 71 double instrumental variable technique (EIVD), can estimate the variance (or
 72 covariance) of random errors, they cannot evaluate the bias of the products. One
 73 primary advantage of collocation analysis is that it does not require a high-quality
 74 reference dataset (Su et al., 2014; Wu et al., 2021). However, a crucial prerequisite for
 75 applying collocation methods is the availability of many spatially and temporally
 76 corresponding datasets. For instance, the classic TC method requires a trio of
 77 independent datasets. Su et al. (2014) used the instrumental regression method and
 78 considered lag-1 time series as the third input, proposing the single instrumental
 79 variable algorithm (IVS). Dong et al. (2019) introduced the lag-1 time series from
 80 both inputs, proposing the double instrumental variable algorithm (IVD) for a more
 81 robust solution. Gruber et al. (2016a) extended the original algorithm to incorporate
 82 more datasets, partially addressing the independence assumption to calculate a portion
 83 of error cross-correlation (ECC) by using the extended collocation (EC) method.
 84 Dong et al. (2020a) further proposed the EIVD method, enabling ECC estimation
 85 using three datasets. Collocation methods have found widespread application in the
 86 evaluation of geophysical variable estimates, including soil moisture (Deng et al.,
 87 2023; Ming et al., 2022), precipitation (Dong et al., 2022; Li et al., 2018), ocean wind
 88 speed (Vogelzang et al., 2022; Ribal and Young, 2020), leaf area index (Jiang et al.,
 89 2017), total water storage (Yin and Park, 2021) sea ice thickness and surface salinity
 90 (Hoareau et al., 2018), and near-surface air temperature (Sun et al., 2021).
 91 Recently, many studies have utilized collocation approaches to evaluate
 92 evapotranspiration products, with the TC method to assess uncertainties. For example,
 93 Barraza Bernadas et al. (2018) considered the uncertainties of ET from the Breathing
 94 Earth System Simulator, BESS (Jiang et al., 2020; Jiang and Ryu, 2016), Moderate
 95 Resolution Imaging Spectroradiometer, MOD16 (Mu et al., 2011), and a hybrid

96 model; Khan et al. (2018) utilized extended triple collocation (ETC) (McColl et al.,
 97 2014) to investigate the reliability of ET from MOD16, The Global Land Data
 98 Assimilation System (GLDAS) (Rodell et al., 2004) and the Global Land Evaporation
 99 Amsterdam Model (GLEAM) (Martens et al., 2017) over East Asia; Li et al. (2022)
 100 employed five collocation methods (e.g., IVS, IVD, TC, EIVD, and EC) to analyze
 101 the uncertainties of ET from ERA5-Land (ERA5L) (Muñoz-Sabater et al., 2021),
 102 GLEAM, GLDAS, FluxCom (Jung et al., 2019), and the Penman-Monteith-Leuning
 103 Evapotranspiration V2 (PMLv2) (Zhang et al., 2019).
 104 Moreover, error information derived from collocation analysis is valuable for merging
 105 multi-source data. This was initially applied by Yilmaz et al. (2012) in the fusion of
 106 multi-source soil moisture products and later improved by Gruber et al. (2017) and
 107 further applied in the production of the European Space Agency Climate Change
 108 Initiative (ESA CCI) global soil moisture product (Gruber et al., 2019). Dong et al.
 109 (2020b) also adopted this approach to fusing multi-source precipitation products. In
 110 the study of evapotranspiration, Li et al. (2023c) and Park et al.(2023) utilized a
 111 weight calculation method that does not consider non-zero ECC and fused multiple
 112 ET products in the Nordic and East Asia, respectively, achieving satisfactory fusion
 113 results.
 114 Although the above studies have demonstrated that collocation analysis can
 115 effectively assess the random error variance of ET products and integrate error
 116 information from multiple data sources, these studies have primarily overlooked a
 117 critical aspect: non-zero ECC between ET products. Li et al. (2022) global ET product
 118 evaluation research revealed clear non-zero ECC conditions between ERA5L,
 119 GLEAM, PMLv2, and FluxCom. In TC analysis, non-zero ECC can result in
 120 significant biases in TC-based results (Yilmaz and Crow, 2014). Furthermore, when
 121 using TC-based error information for fusion, it is crucial to consider the information
 122 related to ECC, as this can help improve the fusion accuracy (Dong et al., 2020b; Kim
 123 et al., 2021b).

It is worth noting that non-zero ECC conditions pose unique challenges. Unlike other violations of mathematical assumptions adopted by TC, they cannot be effectively mitigated through rescaling or compensated for by equal magnitude adjustments across inputs. Thus, the implications of non-zero ECC in the context of merging strategies are a critical consideration often overlooked in previous research. This oversight can lead to significant biases and inaccuracies. We aim to bridge this gap by systematically accounting for non-zero ECC in weight calculation, contributing to a more robust and accurate assessment.

In this study, we proposed a collocation-based data ensemble method, considering non-zero ECC conditions, for merging multiple ET products to create the Collocation-Analyzed Multi-source Ensembled Land Evapotranspiration data, abbreviated as CAMELE. The second section of this paper presents the selected data information for this study. In the third section, we explained the error calculation method for collocation analysis and the weighted calculation method that considered ECC. The fourth section analyzed the global errors of different ET products obtained through these calculations and the distribution patterns of the corresponding weights. We evaluated the accuracy of the fused products and compared them with existing products using reference values from site measurements. In the fifth section, we discussed the inherent errors in the methods, analyzed the ECC between the products, and compared the differences between different fusion schemes. Finally, in the sixth section, we summarized the results obtained from this research.

2. Datasets

We selected five widely used ET products that spanned the period from 1980 to 2022. When selecting these products, our aims are to ensure: (1) consistency in original spatiotemporal resolution among the products: minimize potential downscaling operations and avoid introducing additional errors; (2) having three or more products within the same resolution or period: incorporate more information for effective

fusion; (3) products with extensive global observational sequences: gain basic recognition from the community. While we acknowledge the existence of other higher-precision products, their integration would require either downscaling or upscaling other products, potentially introducing uncertainties. Therefore, we chose the combination outlined in the manuscript. Despite its relatively lower resolution compared to some products, it still contributes to our understanding of ET variations, facilitating advantageous exploration. Furthermore, we incorporated in-situ observations and Lu et al.'s (2021) 's-global 0.25° daily-scale ET product derived using Reliability Ensemble Averaging (denoted as REA) to compare our merged product comprehensively. **Table 1** shows the spatial and temporal resolutions of the input datasets.

Table 1 Summary of evapotranspiration products involved.

Name	Schemes	Resolution	Period	Reference
ERA5-Land	H-TESSSEL	0.1°	hourly	1950-present
GLDAS-2	CLSM/Noah /LSM	0.25°	3-hourly daily	2.0: 1948-2014 2.1: 2000-present 2.2: 2003-present
GLEAM-3.7	GLEAM model	0.25°	daily	3.7a: 1980-2022 3.7b: 2003-2022
PMLv2-v017	Penman- Monteith- Leuning	0.083°	8-day average	2000-2020
FluxCom	Machine learning	0.083°	8-day average	2001-2015

2.1. ERA5-Land

The European Centre for Medium-Range Weather Forecasts (ECMWF) produces the latest advanced ERA5L, a global hourly reanalysis dataset with a spatial resolution of

0.1°. It covers the period from January 1950 until approximately one week before the present (Muñoz-Sabater et al., 2021). ERA5-Land is derived from the land component of the ECMWF climate reanalysis, incorporating numerous improvements over previously released versions. It is based on the Tiled ECMWF Scheme for Surface Exchanges over Land incorporating land surface hydrology (H-TESSEL), utilizing version CY45R1 of the ECMWF's Integrated Forecasting System (IFS). The dataset benefits from atmospheric forcing data, which acts as an indirect constraint on the model-based estimates (Hersbach et al., 2020). The dataset is available through the Climate Change service of the Copernicus Center at <http://cds.climate.copernicus.eu>. Evapotranspiration in ERA5L, defined as "total evaporation," represents the accumulated amount of water that has evaporated from the Earth's surface, including a simplified representation of transpiration from vegetation into the vapor in the air. The soil water and energy balance are computed using standard soil discretization. Readers could consult section 8.6.5 of the IFS documentation (ECMWF, 2014). The original dataset is interpolated from (1801, 3600) to (1800, 3600) using kriging interpolation and then upscaled from an hourly to a daily resolution, changing spatial resolution from 0.1° to 0.25°.

2.2. GLDAS

The Global Land Data Assimilation System (GLDAS) product utilizes advanced data assimilation methodologies, integrating model and observation datasets for land-surface simulations (Rodell et al., 2004). GLDAS employs multiple land-surface models (LSMs), namely Noah, Mosaic, Variable Infiltration Capacity (VIC), and the Community Land Model (CLM). Together, these models generate global evapotranspiration estimates at fine and coarse spatial resolutions (0.01° and 0.25°) and temporal resolutions (3-hourly and monthly). The most recent iteration of GLDAS, version 2, consists of three components: GLDAS-2.0, GLDAS-2.1, and GLDAS-2.2. GLDAS-2.0 relies entirely on the Princeton meteorological forcing input

data, providing a consistent temporal series from 1948 to 2014 (Sheffield et al., 2006). The GLDAS-2.1 simulation commences on January 1, 2000, utilizing the conditions from the GLDAS-2.0 simulation. On the other hand, GLDAS-2.2 is simulated from February 1, 2003, employing the conditions from GLDAS-2.0 and forcing with meteorological analysis fields from the ECMWF Integrated Forecasting System (IFS). Additionally, the GRACE satellite's total terrestrial water anomaly observation is assimilated into the GLDAS-2.2 product (Li et al., 2019a). This study aimed to cover the research period from 1980 to 2022. Non-zero ECC between the transpiration estimates of GLDAS-2.2 and ERA5L has been reported in a recent study (Li et al., 2023a). Considering the similarities in the calculation of ET and transpiration of GLDAS and ERA5L, this report partially indicates a correlation. Therefore, GLDAS-2.0 and GLDAS-2.1 were selected as inputs instead. The "Evap_tavg" parameter representing evapotranspiration is derived from the original products and aggregated to a daily scale. For more detailed information on the GLDAS-2 models, please refer to NASA's Hydrology Data and Information Services Center at <http://disc.sci.gsfc.nasa.gov/hydrology>. Despite the same forcing between GLDAS-2.1 and GLDAS-2.2, significant differences exist between the model results of different GLDAS versions (Qi et al., 2020, 2018; Jiménez et al., 2011). The non-zero ECC will generally still be met between different versions. Thus, we still need to analyze the non-zero ECC situations between ERA5L and GLDAS-2.0 and 2.1, which will be assessed in the discussion sections.

2.3. GLEAM

The version of the Global Land Evaporation Amsterdam Model 3.7 (GLEAM-3.7) dataset (Martens et al., 2017; Miralles et al., 2011) at 0.25° is used. This version of GLEAM provides daily estimations of actual evaporation, bare soil evaporation, canopy interception, transpiration from vegetation, potential evaporation, and snow

sublimation. The third version of GLEAM contains a new DA scheme, an updated water balance module, and evaporative stress functions. Two datasets that differ only in forcing and temporal coverage are provided: GLEAMv3.7a-43-year period (1980 to 2022) based on satellite and reanalysis (ECMWF) data; GLEAMv3.7b-20-year period (2003 to 2022) based on only satellite data. GLEAMv3.7a is used in this study. The data are freely available on the GLEAM website (<https://www.gleam.eu>). The cover-dependent potential evaporation rate (E_p) is calculated using the Priestley-Taylor equation (Priestley and TAYLOR, 1972). Then a multiplicative stress factor is used to convert E_p into actual transpiration and bare soil evaporation, which is the function of microwave vegetation optimal depth (VOD) and root-zone soil moisture. For detailed description, please refer to the paper by Martens et al., (2017). The GLEAM data were validated at 43 FluxNet flux sites and have been proven to provide reliable ET estimations (Majozi et al., 2017).

2.4. PMLv2

The Penman-Monteith-Leuning version 2 global evaporation model (PMLv2) has been developed based on the Penman-Monteith-Leuning model (Zhang et al., 2019; Leuning et al., 2009). Initially proposed by Leuning et al. (2008), the PML model underwent further enhancements by Zhang et al. (2010). The PML version 1 (PMLv1) incorporates a biophysical model that considers canopy physiological processes and soil evaporation to estimate surface conductance accurately (G_s), which is the focus of the PM-based method. This version was subsequently enhanced by incorporating a canopy conductance (G_c) model that couples vegetation transpiration with gross primary productivity, resulting in the development of PML version 2 (PMLv2) as described by Gan et al. (2018). Zhang et al. (2019) applied the PMLv2 model globally. The daily inputs for this model include leaf area index (LAI), broadband albedo, and emissivity obtained from the Moderate Resolution Imaging Spectroradiometer (MODIS), as well as temperature variables (daily maximum temperature- T_{max} , daily

minimum temperature- T_{min} , daily mean temperature- T_{avg}), instantaneous variables (surface pressure- P_{surf} , atmosphere pressure- P_a , wind speed at 10-meter height- U , specific humidity- q), and accumulated variables (precipitation- P_{rcp} , inward longwave solar radiation- R_{ln} , inward shortwave solar radiation- R_s) from GLDAS-2.0. Evaporation is divided into direct evaporation from bare soil (E_s), evaporation from solid water sources (water bodies, snow, and ice) (ET_{water}), and vegetation transpiration (E_c). To ensure its accuracy, the PMLv2-ET model was calibrated against 8-daily eddy covariance data from 95 global flux towers representing ten different land cover types.

In this study, we employ the latest version, v017. The data is freely available through the google earth engine https://developers.google.com/earth-engine/datasets/catalog/CAS_IGSNRR_PML_V2_v017.

2.5. FluxCom

FluxCom is a machine-learning-based approach combining global land-atmosphere energy flux data by combining remote sensing and meteorological data (Jung et al., 2019). To achieve this, FluxCom utilizes various machine-learning regression tools, including tree-based methods, regression splines, neural networks, and kernel methods. The outputs of FluxCom are designed based on two complementary strategies: (1) FluxCom-RS, which exclusively merges remote sensing data to generate high spatial resolution flux data; and (2) FluxCom-RS+METEO, which combines meteorological observations with remote sensing data at a daily temporal resolution. The exclusive use of remote sensing data in the ensemble allows producing gridded flux products at a spatial resolution of 500m, albeit with a relatively low frequency of 8 days. It is important to note that the FluxCom-RS data only covers the period after 2000 due to data availability.

In contrast, the merging of meteorological and remote sensing data extends the coverage back to 1980 at the cost of a coarser spatial resolution of 0.5°. For more

detailed information about the FluxCom dataset, please refer to the FluxCom website (<http://FluxCom.org/>). The data is freely available upon contacting the authors. In this study, we utilized the FluxCom-RS 8-daily 0.0833° energy flux data and converted the latent heat values to ~~evaporation~~ evapotranspiration using ERA5L aggregated daily air temperature. Furthermore, the original ET data were interpolated to a spatial resolution of 0.1° using the MATLAB Gaussian process regression package.

2.6. Global in-situ observation: FluxNet

The latest FluxNet2015 4.0 eddy-covariance data were used in our study (Pastorello et al., 2020). Following the filtering process by Lin et al. (2018) and Li et al. (2019b), firstly, only the measured and good-quality gap-filled data were used for quality control. Secondly, we excluded days with rainfall and the subsequent day after rainy events to mitigate the impact of canopy interception (Medlyn et al., 2017; Knauer et al., 2018). Additionally, previous studies have indicated an energy imbalance problem in FluxNet2015 data. Therefore, following the method proposed by Twine et al. (2000), the measured ET data were corrected using the residual method based on energy balance.

After data filtering and processing, 212 sites are selected as shown in **Figure 1**. The selected sites are distributed globally, primarily in North America and Europe. The International-Geosphere–Biosphere Program (IGBP) land cover classification system (Loveland et al., 1999) was employed to distinguish the 13 Plant Functional Types (PFTs) across sites. The IGBP classification was determined based on metadata from the FluxNet official website, including evergreen needle leaf forests (ENF, 49 sites), evergreen broadleaf forests (EBF, 15 sites), deciduous broadleaf forests (DBF, 26 sites), croplands (CRO, 20 sites), grasslands (GRA, 39 sites), savannas (SAV, 9 sites), mixed forests (MF, 9 sites), closed shrublands (CSH, 3 sites), deciduous needle leaf forests (DNF, 1 site), open shrublands (OSH, 13 sites), snow and ice (SNO, 1 site),

woody savannas (WSA, 6 sites) and permanent wetland (WET, 21 sites). Changes in the IGBP classification during the study period are possible, but such information is not publicly available. Interested parties can obtain relevant information by directly contacting the site coordinators.

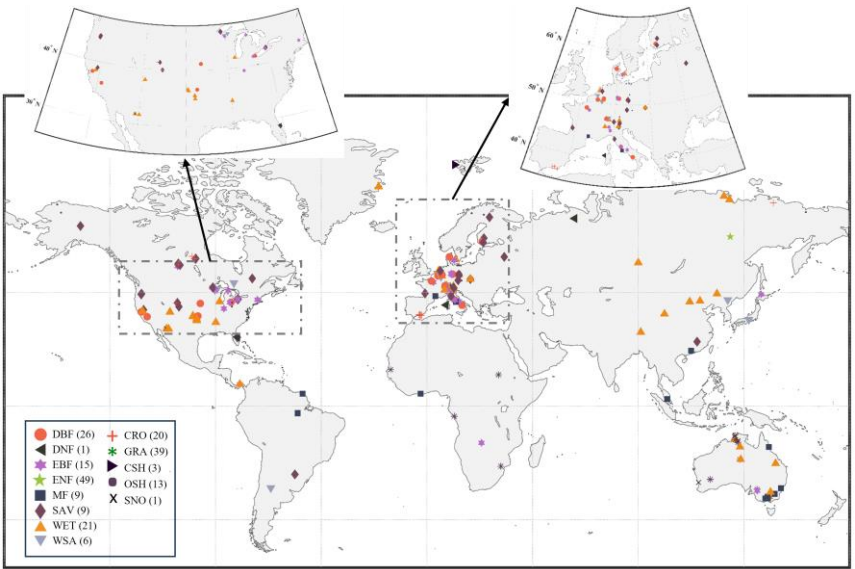


Figure 1 Global distribution of selected FluxNet Sites.

3. Method

In this study, the fusion of products consisted of three steps: (1) the collocation method (IVD and EIVD) was used to calculate the random error variance of the selected input products, determine the regionally optimal products, and set an error threshold; (2) aiming for minimum mean-square-error (MSE), the weights of different products on each grid were calculated; (3) the products were fused according to the weights to obtain a long sequence of evapotranspiration products. Since IVD and EIVD were developed by combining instrumental variable regression and the extended collocation system, a description of TC and EC algorithms was also included.

3.1. Triple collocation analysis

Since its development in 1998, the implications and formulations of the triple collocation problem have been investigated in many studies. Here, we used difference notation for demonstration.

The commonly used error structure for triple collocation analysis (TCA) is:

$$i = \alpha_i + \beta_i \Theta + \varepsilon_i \quad (1)$$

where $i \in [X, Y, Z]$ are three spatially and temporally collocated data sets; Θ is the unknown true signal for relative geographical variable; α_i and β_i are additive and multiplicative bias factors against the true signal, respectively; ε_i is the additive zero-mean random error.

The above structure is also a typical instrumental variable (IV) regression. Thus, this provides another perspective to introduce more variables (>3) (Dong and Crow, 2017; Su et al., 2014) and polynomial models (Yilmaz and Crow, 2013; De Lannoy et al., 2007) to the standard TC. We recommend that the readers refer to Su et al. (2014) for a more detailed discussion on using the IV framework.

The basic assumptions adopted in TC are as follows: (i) Linearity between true signal and data sets, (ii) signal and error stationarity, (iii) independency between random error and true signal (error orthogonality), (iv) independence between random errors (zero ECC). Although many studies have indicated that some of these assumptions are often violated in practice (Li et al., 2018, 2022; Jia et al., 2022), the formulation based on these assumptions is still the most robust implementation (Gruber et al., 2016b). A discussion on these assumptions will be provided in the discussion section.

The data sets first need to be rescaled against an arbitrary reference (e.g., X). The others are scaled through a TC-based rescaling scheme:

$$Y^X = \beta_Y^X (Y - \bar{Y}) + \bar{X} \quad Z^X = \beta_Z^X (Z - \bar{Z}) + \bar{X} \quad (2)$$

The overbar denotes the mean value, and β_Y^X and β_Z^X are the scaling factors as:

$$\begin{cases} \beta_Y^X = \frac{\beta_X}{\beta_Y} = \frac{\langle (X - \bar{X})(Z - \bar{Z}) \rangle}{\langle (Y - \bar{Y})(Z - \bar{Z}) \rangle} = \frac{\sigma_{XZ}}{\sigma_{YZ}} \\ \beta_Z^X = \frac{\beta_X}{\beta_Z} = \frac{\langle (X - \bar{X})(Y - \bar{Y}) \rangle}{\langle (Z - \bar{Z})(Y - \bar{Y}) \rangle} = \frac{\sigma_{XY}}{\sigma_{ZY}} \end{cases} \quad (3)$$

where $\langle \cdot \rangle$ is the average operator, σ_{ij} is the covariance of data sets i and j .

Subsequently, the error variances could be estimated by averaging the cross-multiplied data set differences as follows:

$$\begin{cases} \sigma_{\varepsilon_X}^2 = \langle (X - Y^X)(X - Z^X) \rangle \\ \sigma_{\varepsilon_Y}^2 = \beta_Y^{X^2} \sigma_{\varepsilon_Y}^2 = \langle (Y^X - X)(Y^X - Z^X) \rangle \\ \sigma_{\varepsilon_Z}^2 = \beta_Z^{X^2} \sigma_{\varepsilon_Z}^2 = \langle (Z^X - X)(Z^Y - Y^X) \rangle \end{cases} \quad (4)$$

Expanding the bracket and expressing the rescaling factors yields:

$$\begin{cases} \sigma_{\varepsilon_X}^2 = \sigma_X^2 - \frac{\sigma_{XY}\sigma_{XZ}}{\sigma_{YZ}} \\ \sigma_{\varepsilon_Y}^2 = \sigma_Y^2 - \frac{\sigma_{YX}\sigma_{YZ}}{\sigma_{XZ}} \\ \sigma_{\varepsilon_Z}^2 = \sigma_Z^2 - \frac{\sigma_{ZX}\sigma_{ZY}}{\sigma_{XY}} \end{cases} \quad (5)$$

When selecting various scaling references, it is essential to note that the absolute error variances remain consistent. However, this choice can have an impact on the estimation of data sensitivity to the actual signal ($\beta_i^2 \sigma_\Theta^2$), which serves as a crucial indicator for comparing spatial error patterns. In order to address the reliance on a specific scaling reference, Draper et al. (2013) introduced the fractional root-mean-squared-error ($fMSE_i$). This measure is obtained by normalizing the unscaled error variance with respect to the true signal variance:

$$fMSE_i = \frac{\sigma_{\varepsilon_i}^2}{\sigma_i^2} = \frac{\sigma_{\varepsilon_i}^2}{\beta_i^2 \sigma_\Theta^2 + \sigma_{\varepsilon_i}^2} = \frac{1}{1 + SNR_i} \quad (6)$$

where $SNR_i = \frac{\beta_i^2 \sigma_\Theta^2}{\sigma_{\varepsilon_i}^2} \in [0, 1]$ is the normalized signal-to-noise ratio. $SNR = 0$

indicates a noise-free observation, while $SNR = 1$ corresponds that the variances of estimates equal that of the true signal.

Following similar ideas, Mccoll et al. (2014) extended the framework to estimate the

356 data-truth correlation, known as the ETC:

$$R_i^2 = \frac{\beta_i^2 \sigma_\Theta^2}{\beta_i^2 \sigma_\Theta^2 + \sigma_{\varepsilon_i}^2} = \frac{SNR_i}{1 + SNR_i} \quad (7)$$

$$R_i^2 = 1 - fMSE_i$$

357 In comparison to the conventional coefficient of determination R_{ij} , which is
 358 influenced by data noise and sensitivity. It is important to note that R_i^2 is merely based
 359 on the data set i , whereas R_{ij} is influenced by both data set i and reference j . In other
 360 words, R_i^2 incorporates the dependency on the chosen reference. Thus, TC-derived
 361 $fMSE_i$ and R_i^2 serve as superior indicators for assessing the actual quality of data, as
 362 discussed by Kim et al. (2021b) and Gruber et al. (2020).

363 3.2. Double instrumental variable technique

364 The assumed error structure in TC is also a typical instrumental variable (IV)
 365 regression. In practical usage, finding three completely independent sets of products is
 366 usually tricky. Su et al. (2014) effectively improve the applicability of the TC method
 367 by using the lag-1 time series (e.g., $X_{t-1} = \alpha_X + \beta_X \Theta_{t-1} + \varepsilon_{X,t-1}$) from one of the
 368 two sets of data as the third input for TC. In this way, we only need two independent
 369 products for input.

370 Such process includes another assumption that all data sets contain serially white
 371 errors (i.e., $\langle \varepsilon_{i,t} \varepsilon_{i,t-1} \rangle = 0$, zero auto-correlation). Building upon this, Dong et al.
 372 (2019) utilizes the lag-1 time series from both data sets as inputs and propose the
 373 more stable IVD method.

374 For a double input $[X, Y]$ with $\sigma_{\varepsilon_X \varepsilon_Y} = 0$, the linear error model and related lag-1
 375 time series can be expressed as:

$$\begin{cases} X = \alpha_X + \beta_X \Theta + \varepsilon_X \\ Y = \alpha_Y + \beta_Y \Theta + \varepsilon_Y \end{cases} \quad \begin{cases} I = \alpha_X + \beta_X \Theta_{t-1} + \varepsilon_{X,t-1} \\ J = \alpha_Y + \beta_Y \Theta_{t-1} + \varepsilon_{Y,t-1} \end{cases} \quad (8)$$

376 where I and J are the lag-1 time series of X and Y , respectively.

377 Assuming product errors are mutually independent and orthogonal to the truth, the

378 covariance between the products is expressed as:

$$\begin{cases} \sigma_X^2 = \beta_X^2 \sigma_\Theta^2 + \sigma_{\varepsilon_X}^2 & \sigma_Y^2 = \beta_Y^2 \sigma_\Theta^2 + \sigma_{\varepsilon_Y}^2 \\ \sigma_{XY} = \beta_X \beta_Y \sigma_\Theta^2 \\ \sigma_{IX} = \beta_X^2 L_{\Theta\Theta} & \sigma_{JY} = \beta_Y^2 L_{\Theta\Theta} \end{cases} \quad (9)$$

379 where $L_{ii} = \langle i_t i_{t-1} \rangle$ is the auto-covariance. Therefore, the IVD-estimated dynamic
380 range ratio scaling factors yields:

$$s_{ivd} \equiv \frac{\beta_X}{\beta_Y} = \sqrt{\frac{\sigma_{IX}}{\sigma_{JY}}} \quad (10)$$

381 Hence, the random error variances of X and Y can be solved as:

$$\begin{cases} \sigma_{\varepsilon_X}^2 = \sigma_X^2 - \sigma_{XY} * s_{ivd} \\ \sigma_{\varepsilon_Y}^2 = \sigma_Y^2 - \frac{\sigma_{XY}}{s_{ivd}} \end{cases} \quad (11)$$

382 3.3. Extended double instrumental variable technique

383 Furthermore, by adopting the designed matrix in the EC method (Gruber et al., 2016a),
384 Dong et al. (2020a) present the EIVD method to estimate the error variance matrix
385 with only two independent data sets.

386 For a triplet input $[i, j, k]$ with $\sigma_{\varepsilon_i \varepsilon_j} \neq 0$. The dynamic range ratio scaling factors can
387 be estimated as follows:

$$s_{ij} \equiv \frac{\beta_i}{\beta_j} = \sqrt{\frac{L_{ii}}{L_{jj}}} \quad (12)$$

388 where $L_{ii} = \langle i_t i_{t-1} \rangle$ is the auto-covariance of inputs. Subsequently, the sensitivity
389 and absolute error variance of the data set follow:

$$\beta_j^2 \sigma_\Theta^2 = \sigma_{ij} \sqrt{\frac{L_{ii}}{L_{jj}}} \quad \sigma_{\varepsilon_j}^2 = \sigma_{ij} \sqrt{\frac{L_{ii}}{L_{jj}}} - \sigma_i^2 \quad (13)$$

390 The cross-multiplied factors can be estimated by:

$$\beta_i \beta_j \sigma_\Theta^2 = \sigma_{ik} \sqrt{\frac{L_{jj}}{L_{kk}}} = \sigma_{jk} \sqrt{\frac{L_{ii}}{L_{kk}}} \quad \sigma_{\varepsilon_i \varepsilon_j} = \sigma_{ij} - \beta_i \beta_j \sigma_\Theta^2 \quad (14)$$

Hence, for a triplet with the input of $[X, Y, Z]$ with $\sigma_{\varepsilon_X \varepsilon_Y} \neq 0$: the matrix notation of the above system with $\mathbf{y} = \mathbf{Ax}$ is given as:

$$\mathbf{y} = \begin{pmatrix} \sigma_X^2 \\ \sigma_Y^2 \\ \sigma_Z^2 \\ \sigma_{XY} \sqrt{\frac{L_{XX}}{L_{ZZ}}} \\ \sigma_{XZ} \sqrt{\frac{L_{XX}}{L_{ZZ}}} \\ \sigma_{YZ} \sqrt{\frac{L_{YY}}{L_{ZZ}}} \\ \sigma_{ZX} \sqrt{\frac{L_{ZZ}}{L_{XX}}} \\ \sigma_{ZY} \sqrt{\frac{L_{ZZ}}{L_{YY}}} \\ \sigma_{XZ} \sqrt{\frac{L_{YY}}{L_{ZZ}}} \\ \sigma_{YZ} \sqrt{\frac{L_{XX}}{L_{ZZ}}} \end{pmatrix}_{10 \times 1} \quad \mathbf{A} = \begin{pmatrix} \mathbf{I}_{4 \times 4} & \mathbf{I}_{4 \times 4} \\ \mathbf{0}_{6 \times 4} & \mathbf{0}_{6 \times 4} \end{pmatrix}_{10 \times 8} \quad \mathbf{x} = \begin{pmatrix} \beta_X^2 \sigma_\theta^2 \\ \beta_Y^2 \sigma_\theta^2 \\ \beta_Z^2 \sigma_\theta^2 \\ \beta_X \beta_Y \sigma_\theta^2 \\ \sigma_{\varepsilon_X}^2 \\ \sigma_{\varepsilon_Y}^2 \\ \sigma_{\varepsilon_Z}^2 \\ \sigma_{\varepsilon_X \varepsilon_Y} \end{pmatrix}_{8 \times 1} \quad (15)$$

Likewise, the least-squared solution for unknown \mathbf{x} is then solved by:

$$\mathbf{x} = (\mathbf{A}^T \mathbf{A})^{-1} \mathbf{A}^T \mathbf{y} \quad (16)$$

3.4. Weight Estimation

Our objective is to predict an uncertain variable, such as evapotranspiration (ET) over time at a specific location, by utilizing parent products that may contain random errors. The underlying concept of weighted averaging is to extract independent information from multiple data sources to enhance prediction accuracy by mitigating the effects of random errors. The effectiveness of this approach relies on the independence of the individual data sources under consideration. Weighted averaging has found applications in various fields following the influential work of Bates and Granger (1969), who proposed the optimal combination of forecasts based on a minimum MSE criterion. In this context, the term "optimal" refers to minimizing the variance of residual random errors in the least squares sense. Mathematically, this weighted

average can be expressed as follows:

$$\bar{x} = \bar{\mathbf{W}}^T \bar{\mathbf{X}} = \sum_{i=1}^N \omega_i x_i \quad (17)$$

where \bar{x} is the merged estimate; $\bar{\mathbf{X}} = [x_1, \dots, x_n]^T$ contains the temporally collocated estimates from N different parent products, which are merged with relative zero-mean random error $\bar{\mathbf{e}} = [\varepsilon_1, \dots, \varepsilon_n]^T$; and $\bar{\mathbf{W}} = [\omega_1, \dots, \omega_n]^T$ contains the weights assigned to these estimates, where $\omega_i \in [0,1]$ and $\sum \omega_i = 1$ ensuring an unbiased prediction. The averaging weights can be expressed as the solution to the problem:

$$\min f(\bar{\mathbf{W}}) = \mathbb{E}(\bar{\mathbf{e}}^T \bar{\mathbf{W}})^2 \quad (18)$$

where $\mathbb{E}()$ is the operator for mathematical expectation, the solution of this problem is determined by the individual random error characteristics of the input data sets and can be derived from their covariance matrix (Bates and Granger, 1969; Gruber et al., 2017; Kim et al., 2021b):

$$\begin{aligned} \bar{\mathbf{W}} &= (\bar{\mathbf{I}}^T \mathbb{E}(\bar{\mathbf{e}} \bar{\mathbf{e}}^T)^{-1} \bar{\mathbf{I}})^{-1} \mathbb{E}(\bar{\mathbf{e}} \bar{\mathbf{e}}^T)^{-1} \bar{\mathbf{I}} \\ \sigma_{\bar{\varepsilon}_x}^2 &= (\bar{\mathbf{I}}^T \mathbb{E}(\bar{\mathbf{e}} \bar{\mathbf{e}}^T)^{-1} \bar{\mathbf{I}})^{-1} \end{aligned} \quad (19)$$

where $\mathbb{E}(\bar{\mathbf{e}} \bar{\mathbf{e}}^T)$ is the $N \times N$ error covariance matrix that holds the random error variance $\sigma_{\varepsilon_i}^2$ of the parent products in the diagonals and relative error covariances $\sigma_{\varepsilon_i \varepsilon_j}$ in the off-diagonals; $\bar{\mathbf{I}} = [1, \dots, 1]^T$ is an ones-vector of length N ; and $\sigma_{\bar{\varepsilon}_x}^2$ is the resulting random error variances of the merged estimate.

When only two groups of products are used as input ($N = 2$), it is generally assumed that the errors between them are independent. In this case, the weights are as follows:

$$\begin{aligned} \mathbb{E}(\bar{\mathbf{e}} \bar{\mathbf{e}}^T) &= \begin{bmatrix} \sigma_{\varepsilon_1}^2 & 0 \\ 0 & \sigma_{\varepsilon_2}^2 \end{bmatrix} \\ \omega_1 &= \frac{\sigma_{\varepsilon_2}^2}{\sigma_{\varepsilon_1}^2 + \sigma_{\varepsilon_2}^2} \quad \omega_2 = \frac{\sigma_{\varepsilon_1}^2}{\sigma_{\varepsilon_1}^2 + \sigma_{\varepsilon_2}^2} \end{aligned} \quad (20)$$

In most cases, we can identify three sets of products as inputs ($N = 3$). In this scenario, we consider the possibility of error homogeneity, assuming a non-zero ECC

exists between inputs 1 and 2. In this case, the error matrix can be represented as:

$$\mathbb{E}(\vec{e}\vec{e}^T) = \begin{bmatrix} \sigma_{\varepsilon_1}^2 & \sigma_{\varepsilon_1\varepsilon_2} & 0 \\ \sigma_{\varepsilon_1\varepsilon_2} & \sigma_{\varepsilon_2}^2 & 0 \\ 0 & 0 & \sigma_{\varepsilon_3}^2 \end{bmatrix} \quad (21)$$

The weights can then be written as:

$$\vec{W} = \begin{bmatrix} \frac{\sigma_{\varepsilon_2}^2 - \sigma_{\varepsilon_1\varepsilon_2}}{(\sigma_{\varepsilon_1}^2\sigma_{\varepsilon_2}^2 - \sigma_{\varepsilon_1\varepsilon_2}^2) * \mathbb{Z}} \\ \frac{\sigma_{\varepsilon_1}^2 - \sigma_{\varepsilon_1\varepsilon_2}}{(\sigma_{\varepsilon_1}^2\sigma_{\varepsilon_2}^2 - \sigma_{\varepsilon_1\varepsilon_2}^2) * \mathbb{Z}} \\ \frac{1}{\sigma_{\varepsilon_3}^2 * \mathbb{Z}} \end{bmatrix} \quad (22)$$

$$\mathbb{Z} = \frac{\sigma_{\varepsilon_1}^2 + \sigma_{\varepsilon_2}^2 - 2\sigma_{\varepsilon_1\varepsilon_2}}{\sigma_{\varepsilon_1}^2\sigma_{\varepsilon_2}^2 - \sigma_{\varepsilon_1\varepsilon_2}^2} + \frac{1}{\sigma_{\varepsilon_3}^2}$$

It is essential to acknowledge that before applying these weights for merging the data sets, it is necessary to address any existing systematic differences. Typically, this is achieved by rescaling the data sets to a standardized data space. Consequently, the weights can be derived from the rescaled data sets using Eq (2)-(3) and converge accordingly. This procedure ensures the accuracy and reliability of the merged data sets for further analysis.

If ECC is not considered (i.e., setting $\sigma_{\varepsilon_1\varepsilon_2} = 0$), Eq (22) represents the weight calculation method commonly used in most TC fusion studies. In contrast to the fusion studies mentioned above for evapotranspiration products, for the first time, the consideration of non-zero ECC is incorporated into the fusion process and integrated into the weight calculation. Yilmaz and Crow (2014) have demonstrated that TC underestimates error variances when the zero ECC assumption is violated. Li et al. (2022), in their evaluation study of global ET products using the collocation method, also indicated the existence of error homogeneity issues between commonly used ET products (such as ERA5L and GLEAM), necessitating the consideration of the influence of non-zero ECC. The merging technique employed in this study provides a more explicit characterization of product errors and facilitates the derivation of more

reliable weight coefficients, thereby achieving promising fusion outcomes. The differences in results are evaluated at the site scale by contrasting the scenarios without considering non-zero ECC and directly using simple averages to compare and validate the advantages of the weight calculation method used in our study.

3.5. Merging combination

In this study, we employ five commonly used global land surface ET products as described in the datasets section. PMLv2 and FluxCom-RS have an original resolution of 0.083° and an 8-day average. In this research, they are interpolated to 0.1° resolution, and the values for each data period of 8 days are kept consistent. For example, the values for March 5 to March 12, 2000, are the same. ET values often exhibit variability over an 8-day period, making the use of an 8-day average to represent temporal dynamics potentially introducing further uncertainties. This operation is performed to ensure adequate data for the collocation analysis (Kim et al., 2021a). We openly acknowledge the possible sources of error and express our commitment to addressing and improving them in future work.

As mentioned in the methodology section, it is vital to consider the issue of random error homogeneity among different products before applying the collocation method. Although EC or EIVD methods can be used to calculate the ECC between specific pairs of products, it is necessary to determine which pairs of products have non-zero ECC conditions. In previous research, Li et al.(2022) employed five collocation methods (IVS/IVD/TC/EIVD/EC) to analyze the performance of five sets of ET products (ERA5L/ PMLv2/FluxCom/GLDAS2/GLEAMv3) at the global scale, and applied EC and EIVD methods to calculate the ECC between different products. The results indicated a relatively significant error homogeneity between PMLv2 and FluxCom at a resolution of 0.1° (with a global average ECC of approximately 0.3). The error homogeneity could be attributed to both products utilizing GLDAS meteorological data as input, despite their different methods for ET estimation. At a

resolution of 0.25° , ERA5L and GLEAM exhibited a more apparent error correlation (with a global average ECC of approximately 0.4). Considering the long temporal data of GLEAMv3 version a, ECMWF meteorological data was chosen as the driving force, making the error correlation between the two products predictable. Therefore, this study assumes that non-zero ECC situations occur between PMLv2-FluxCom and ERA5L-GLEAM. We also calculated the possible ECC situations among other products, presented in the discussion section and the appendix. Based on the analysis, our assumed non-zero ECC situations align reasonably well with the actual circumstances.

In addition, previous research suggests that the IVD method outperforms the IVS method in scenarios involving two sets of inputs, while the EIVD method is considered more reliable than the TC method in situations with three sets of inputs (Li et al., 2022; Kim et al., 2021a). Therefore, in this study, the IVD and EIVD methods are selected for computation based on different combinations of inputs. [Table 2](#) presents the data and methods used during corresponding periods. When only two sets of products are available, we employ the IVD method for fusion and calculate weights using Eq. (20). When three sets of products are available, we utilize the EIVD method for fusion and calculate weights using Eq. (22).

Table 2 Combination of inputs and accessible methods

Scenario 1 (0.1°)		
Period	Selected Inputs	Method
(2000.02.26-2000.12.31)	ERA5L/ PMLv2	IVD
(2001.01.01-2015.12.27)	ERA5L/ FluxCom/ PMLv2	EIVD
(2015.12.28-2020.12.26)	ERA5L/ PMLv2	IVD
Scenario 2 (0.25°)		
Period	Selected Inputs	Method
(1980.01.01-1999.12.31)	ERA5L/ GLDAS20/ GLEAMv3.7a	EIVD
(2000.01.01-2022.12.31)	ERA5L/ GLDAS21/ GLEAMv3.7a	

It should be noted that the same product can have different versions. In this study,

appropriate versions are selected based on the following principles: (1) Selection based on the corresponding data coverage duration and ensuring more products to gain more information; (2) Choosing the latest version while considering the assumption of non-zero ECC conditions; (3) Making efforts to select the exact product versions for different periods, to avoid uncertainties caused by version changes. We selected a subset of sites to compare the fusion results using different versions, and the corresponding details will be presented in the discussion section.

3.6. Evaluation indices

Five statistical indicators, namely Root-mean-squared-error (*RMSE*), Pearson's correlation coefficient (*R*), Mean-absolute-error (*MAE*), unbiased *RMSE* (*ubRMSE*) and Kling-Gupta Efficiency (*KGE*), are selected for comparison with existing products. The relative equations are shown as follows:

$$RMSE = \sqrt{\frac{\sum_{i=1}^n (sim_i - obs_i)^2}{n}} \quad (23)$$

$$R = \frac{\sum_{i=1}^n (sim_i - \overline{sim})(obs_i - \overline{obs})}{\sqrt{\sum_{i=1}^n (sim_i - \overline{sim})^2 \sum_{i=1}^n (obs_i - \overline{obs})^2}} \quad (24)$$

$-1 \leq R \leq 1$

$$MAE = \frac{1}{n} \sum_{i=1}^n |sim_i - obs_i| \quad (25)$$

$$ubRMSE = \sqrt{\frac{\sum_{i=1}^n \left[\frac{(sim_i - \overline{sim}) - (obs_i - \overline{obs})}{n} \right]^2}{n}} \quad (26)$$

Where *sim* is the simulations, *obs* is the observation as reference.

The modified *KGE* (Kling et al., 2012) offers insights into reproducing temporal dynamics and preserving the distribution of time series, which are increasingly used to calibrate and evaluate hydrological models (Knoben et al., 2019). For a better understanding of the *KGE* statistic and its advantages over the Nash-Sutcliffe Efficiency (*NSE*), please refer to Gupta et al. (2009). The equation is given by:

$$KGE = 1 - \sqrt{(r - 1)^2 + \left(\frac{\sigma_{sim}}{\sigma_{obs}} - 1\right)^2 + \left(\frac{\sigma_{sim}/\mu_{sim}}{\sigma_{obs}/\mu_{obs}} - 1\right)^2} \quad (27)$$

Where σ_{obs} and σ_{sim} are the standard deviations of observations and simulations; μ_{obs} and μ_{sim} are the mean of observations and simulations. Similar to *NSE*, $KGE = 1$ indicates perfect agreement of simulations, while $KGE < 0$ reveals that the average of observations is better than simulations (Towner et al., 2019).

4. Results

In this study, we aimed to compare and evaluate the performance of fused products at both site and global scales. At the site scale, the performance of the fused products was evaluated against 212 FluxNet observations and compared with other products, including the simple average. At the global scale, the mean and temporal variations of the land surface ET calculated by the fused products were compared with those of other products.

4.1. Analysis of error variances and weights

This section examines the random error variances and identifies the predominant product based on assigned weights for the 0.1° and 0.25° inputs obtained through the EIVD method.

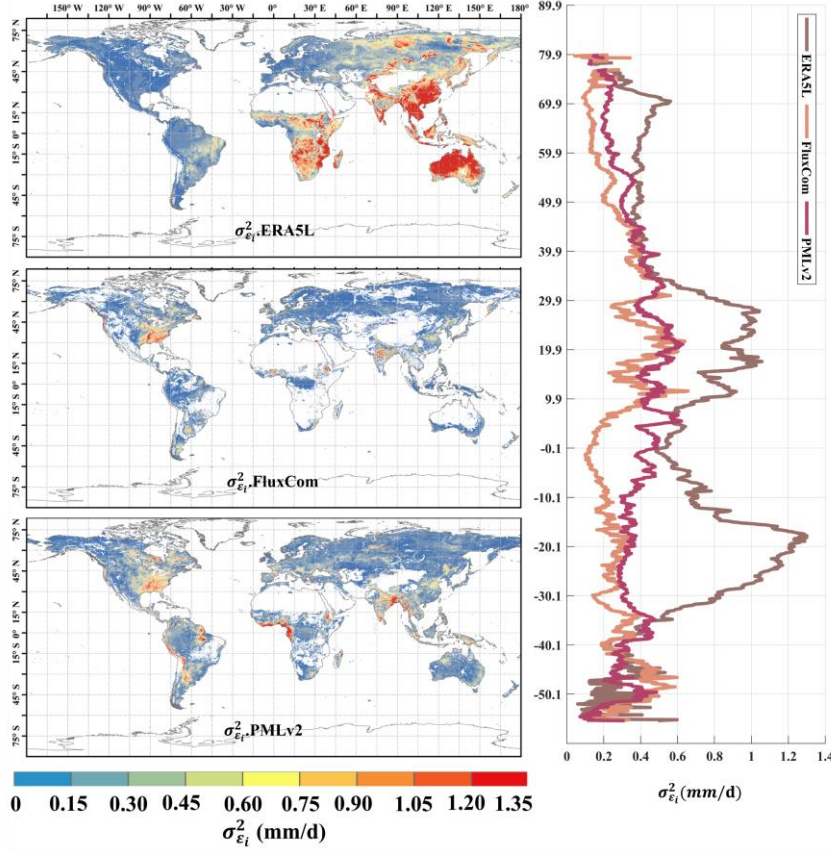


Figure 2 Global distribution of absolute error variances ($\sigma_{\varepsilon_i}^2$) of ERA5L, FluxCom, and PMLv2 using EIVD at 0.1° from 2001 to 2015, depicted alongside corresponding variation curves of average $\sigma_{\varepsilon_i}^2$ with latitude.

Figure 2Figure 2 represents the random errors of the correlation products calculated using the EIVD method from 2001 to 2015 at 0.1° , where a non-zero ECC is assumed between FluxCom and PMLv2. The areas with missing values are due to the absence of data from either FluxCom or PMLv2 in those regions. The global random error variances (mean \pm standard deviation) obtained using the EIVD method are as follows: ERA5L: 0.58 ± 0.53 mm/day, FluxCom: 0.12 ± 0.13 mm/day, PMLv2: 0.17 ± 0.14 mm/day. These results indicate that FluxCom performs best overall, while ERA5L performs the poorest. Regarding spatial distribution, regions with more significant

534 random errors in ERA5L are mainly located in East Asia, Australia, and southern
535 Africa. On the other hand, FluxCom and PMLv2 show relatively more considerable
536 uncertainties in the southeastern United States. The latitude distribution reveals that
537 ERA5L has the highest uncertainty, primarily in the vicinity of 20° to 30° north and
538 south, consistent with its spatial distribution.

539 It is important to note that due to missing data in specific regions at 0.1°, such as
540 Northern Africa, the Sahara Desert region, Northwestern China, and Australia, the
541 error results obtained may not accurately reflect the performance of FluxCom and
542 PMLv2 in these areas. Considering the current results, we can cautiously conclude
543 that FluxCom and PMLv2 demonstrate better performance. Future data
544 supplementation in these regions would further enhance our ability to analyze the
545 products' accuracy.

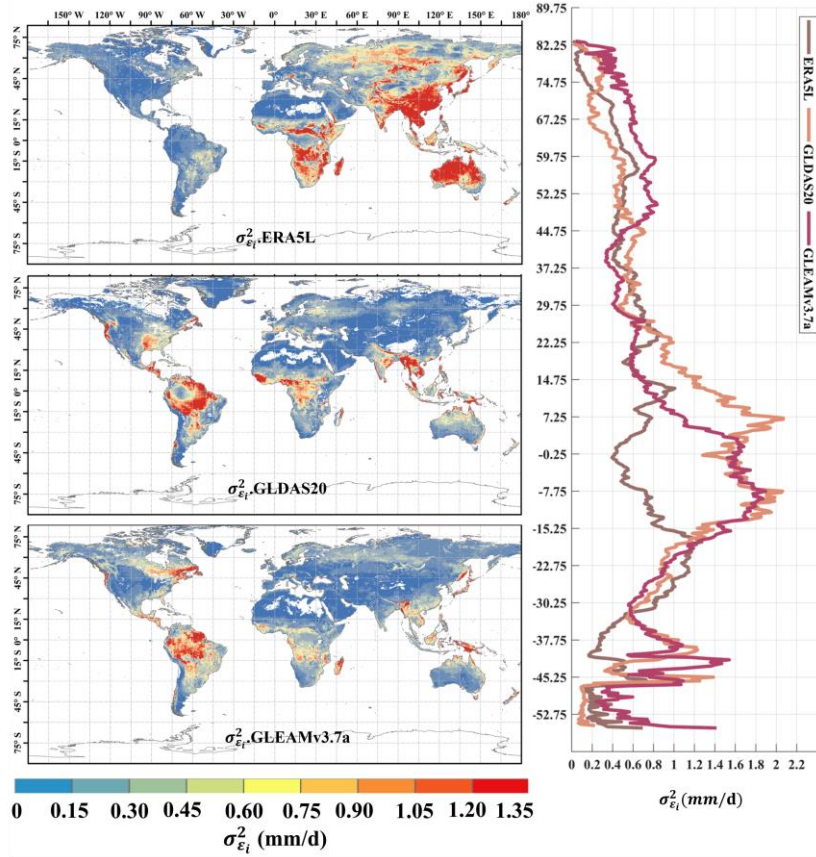


Figure 3 Global distribution of absolute error variances ($\sigma_{\epsilon_i}^2$) of ERA5L, GLDAS2.0, and GLEAMv3.7a using EIVD at 0.25° from 1980 to 1999, depicted alongside corresponding variation curves of average with latitude.

The distribution of random error variance for ERA5L (0.59 ± 0.58 mm/d), GLDAS2.0 (0.37 ± 0.44 mm/d), and GLEAMv3.7a (0.38 ± 0.36 mm/d) from 1980 to 1999 at 0.25° is shown in **Figure 3**. Here, we assumed a non-zero ECC between ERA5L and GLEAM. The ERA5L data was resampled from a 0.1° resolution to 0.25°, and its error distribution pattern is like that of the 0.1° resolution. It exhibits higher uncertainties in East Asia, Australia, and southern Africa. GLDAS and GLEAM exhibit relatively higher uncertainty over the southeastern United States and the Amazon Plain. GLDAS and GLEAM show similar performance among the three

products, while ERA5L performs relatively worse. Regarding the average distribution with latitude, ERA5L demonstrates a more even distribution, whereas GLDAS and GLEAM exhibit relatively higher uncertainties in tropical regions. The ET calculations in both GLDAS and GLEAM involve complex surface parameterization processes. In tropical regions, the high non-heterogeneity in land covers poses a challenge, and the 0.25° resolution grid may not capture the intricacies of the underlying surface conditions. This mismatch could impact the parameterization process, leading to errors. Future work could involve in-depth model analyses or sensitivity experiments to identify sources of error in complex ET models, facilitating improvements.

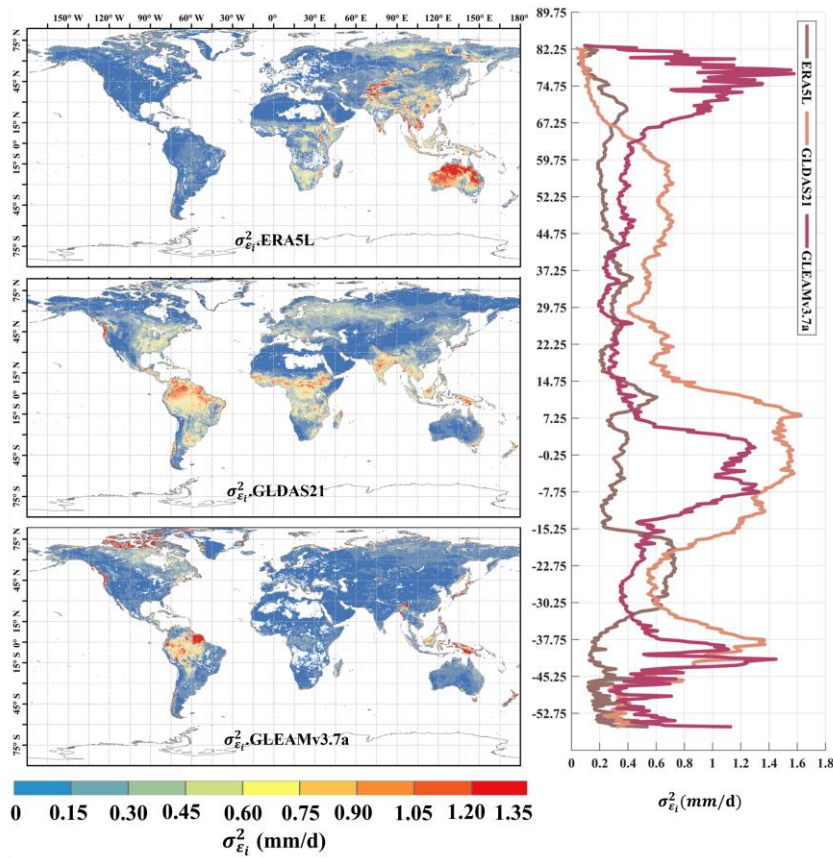


Figure 4 Global distribution of absolute error variances ($\sigma_{\epsilon_l}^2$) of ERA5L, GLDAS2.1,

and GLEAMv3.7a using EIVD at 0.25° from 2000 to 2022, depicted alongside corresponding variation curves of average with latitude.

In addition, [Figure 4](#) presents the distribution of random error variance for ERA5L (0.32 ± 0.33 mm/d), GLDAS2.1 (0.35 ± 0.29 mm/d), and GLEAMv3.7a (0.38 ± 0.36 mm/d) from 2000 to 2022 at a resolution of 0.25°. The non-zero ECC assumption was made between ERA5L and GLEAM. In this combination, ERA5L shows significantly lower errors than in previous periods, indicating improved ERA5L performance during this time frame. However, ERA5L still exhibits more significant errors in the East Asia and Australia regions compared to the other two datasets. The overall errors for GLDAS and GLEAM have also decreased, but there are still random error variances exceeding 1.0 mm/d in the Amazon plain and Indonesia region. Regarding the latitudinal distribution, ERA5L shows relatively smooth changes, while GLDAS and GLEAM exhibit similar trends. However, GLEAM demonstrates a noticeable increase in errors near the Arctic.

Next, in [Figure 5](#), we present the dominant product for each grid cell in the three scenarios, where dominance refers to the product with the highest assigned weight. The results in [Figure 5](#) indicate that at 0.1° resolution, the weights for FluxCom and PMLv2 are significantly higher than ERA5L, aligning with the error calculations presented in [Figure 2](#). This underscores the effectiveness of error and weight analysis based on collocation in reflecting product performance, thereby allowing for a rational adaptation of weights. At 0.25° resolution, the dominant regions for ERA5L, GLDAS-2, and GLEAM products are relatively balanced. In the fusion scenario from 1980 to 1999, GLDAS20 predominantly covers the Northern Hemisphere, while GLEAM dominates the Southern Hemisphere, with ERA5L prevalent in the Amazon region. However, in the fusion scenario from 2000 to 2022, GLEAM's dominant region significantly expanded, primarily covering the central United States and southeastern China. The Amazon region continues to be dominated by ERA5L. The variation in dominant products highlights that the

598 calculation of product weights evolves with changes in the fusion scenario. The error
599 and weight computation methods based on collocation can only provide the minimum
600 MSE solution for a given combination of inputs. It is important to note that changes in
601 inputs will impact the results.

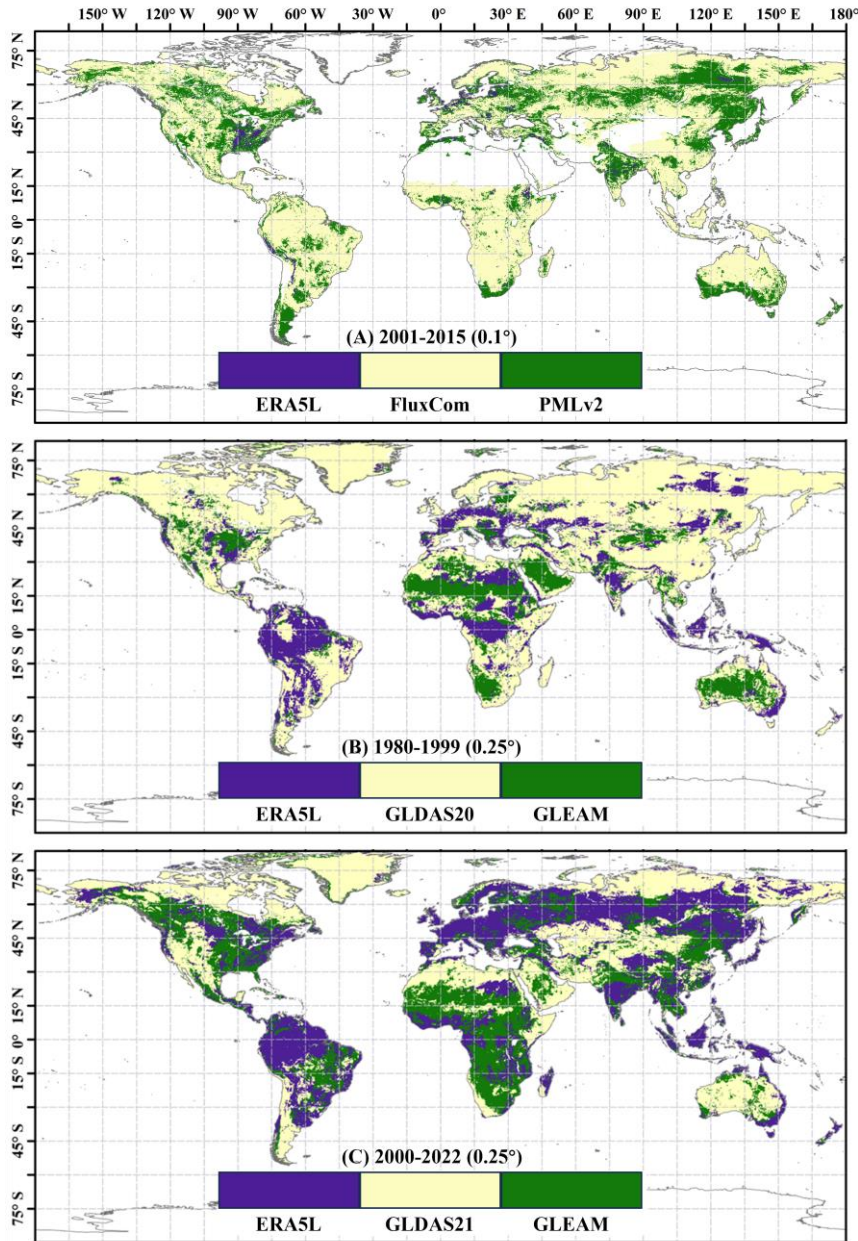


Figure 5 Map of the prevailing product at individual pixels based on scenario-specific weights.

For the analysis at a resolution of 0.1°, we also applied the IVD method to calculate

the errors between ERA5L and PMLv2 for two time periods: 2000 and 2015 to 2020. Since the analysis of product errors is not the focus of this paper, we provide the results of the IVD in the appendix. Grids with higher random error variances correspond to smaller weights when calculating the weights. The weight distribution calculated at different time intervals is available in the appendix.

4.2. Site-scale evaluation and comparison

At the site scale, the performance of CAMELE was compared with FluxNet as the reference. In this subsection, Figure 6 and Table 3 correspond to each other, as they integrate data from 212 sites for all available periods, allowing for a comparative analysis of the performance of different products at different times. Similarly, Figure 7 and Table 4 correspond to each other, where different product metrics were calculated for each site, and the calculated metric results were subjected to statistical analysis.

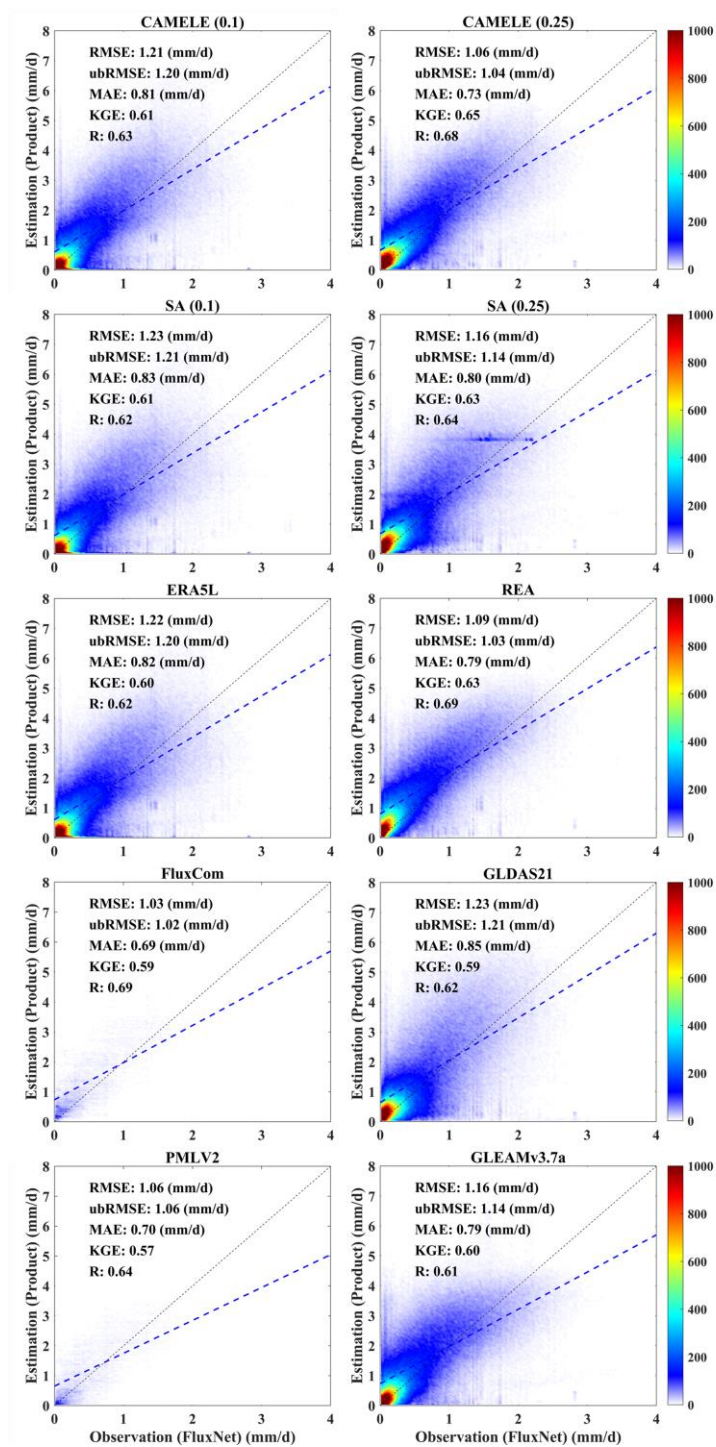


Figure 6 Scatter plots of product corresponding to the available period data from 212 FluxNet sites. The colorbar represents the density, with darker colors indicating higher concentration. The left and right columns present results for 0.1° and 0.25° resolutions, respectively, with "SA" indicating the results for simple average.

Relevant statistical metrics are annotated in their respective figures.

The scatter plots in **Figure 6** demonstrate that CAMELE consistently performs at 0.1° and 0.25° resolutions. At 0.1° resolution, FluxCom and PMLv2 showed superior performance with fewer data points due to their original 8-day average resolution. CAMELE exhibited a performance like ERA5L. At 0.25° resolution, CAMELE performed comparably to the other datasets, demonstrating reasonable accuracy. Notably, there was an improvement in the KGE and R indices. The fitted line closely approximated the 1:1 line, indicating a solid agreement with the observed values. Moreover, the results obtained from the simple average were also acceptable, but SA (0.25°) had a concentration of data points between (2-4 mm/d), possibly due to the inputs having a high concentration within that range. The assumption that a simple average implies equal performance of each product on every grid cell is inaccurate; variations in performance exist among different products across distinct grid cells (regions).

Table 3 Average values of different metrics for CAMELE and other fusion schemes corresponding to the available period data from 212 FluxNet sites. The bolded sections indicate the schemes with the best performance in their respective metrics.

	Product	RMSE (mm/d)	ubRMSE (mm/d)	MAE (mm/d)	KGE	R
0.1°-daily	CAMELE	1.21	1.20	0.81	0.61	0.63
	SA	1.23	1.21	0.83	0.61	0.62
	ERA5L	1.22	1.20	0.82	0.60	0.62
	FluxCom	1.03	1.02	0.69	0.59	0.69
	PMLv2	1.06	1.06	0.70	0.57	0.64
0.25°-daily	CAMELE	1.06	1.04	0.73	0.65	0.68
	SA	1.16	1.14	0.80	0.63	0.64

REA	1.09	1.03	0.79	0.63	0.69
GLDAS21	1.23	1.21	0.85	0.59	0.62
GLEAMv3.7a	1.16	1.14	0.79	0.60	0.61

The information in [Table 3](#) corresponds to [Figure 6](#) and presents the results of various product indicators. The bolded parts indicate the products with the best corresponding indicators. The results indicate that CAMELE performed well at both 0.1° and 0.25° resolutions, mainly showing improvements in the KGE and R indicators. FluxCom exhibited the best performance; however, considering that this product utilized FluxNet sites for result calibration, this phenomenon is reasonable. In this study, we pooled the data from all 212 available periods at the stations as a reference without considering the differences between individual sites. This approach provided an initial validation of the reliability of CAMELE at all sites.

The information in [Figure 7](#) corresponds to the data presented in [Table 4](#), which involves the calculation of five indicators at each site, followed by statistical analysis of these indicators. From the distribution of the violin plots, it can be observed that a violin plot with a closer belly to 1 indicates better results in terms of the R and KGE indicators. CAMELE performs well overall, closely resembling PMLv2 and FluxCom. On the other hand, the results obtained from the Simple Average are relatively poorer. Regarding the RMSE, ubRMSE, and MAE indicators, a violin plot with a closer belly to 0 suggests less errors. CAMELE demonstrates a notable enhancement in performance at the 0.1° level. This suggests that the fusion method effectively reduces errors, aligning with the original intention of weight calculation, and it compares favorably with the products used in the merging scheme. Additionally, FluxCom and PMLv2 also exhibit minimal errors, which is expected considering their utilization of FluxNet sites for error correction. Furthermore, SA shows significantly larger errors. Although the simple average method can compensate for positive and negative errors between inputs in some instances, it can also lead to error accumulation, as evidenced by the results in the violin plots.

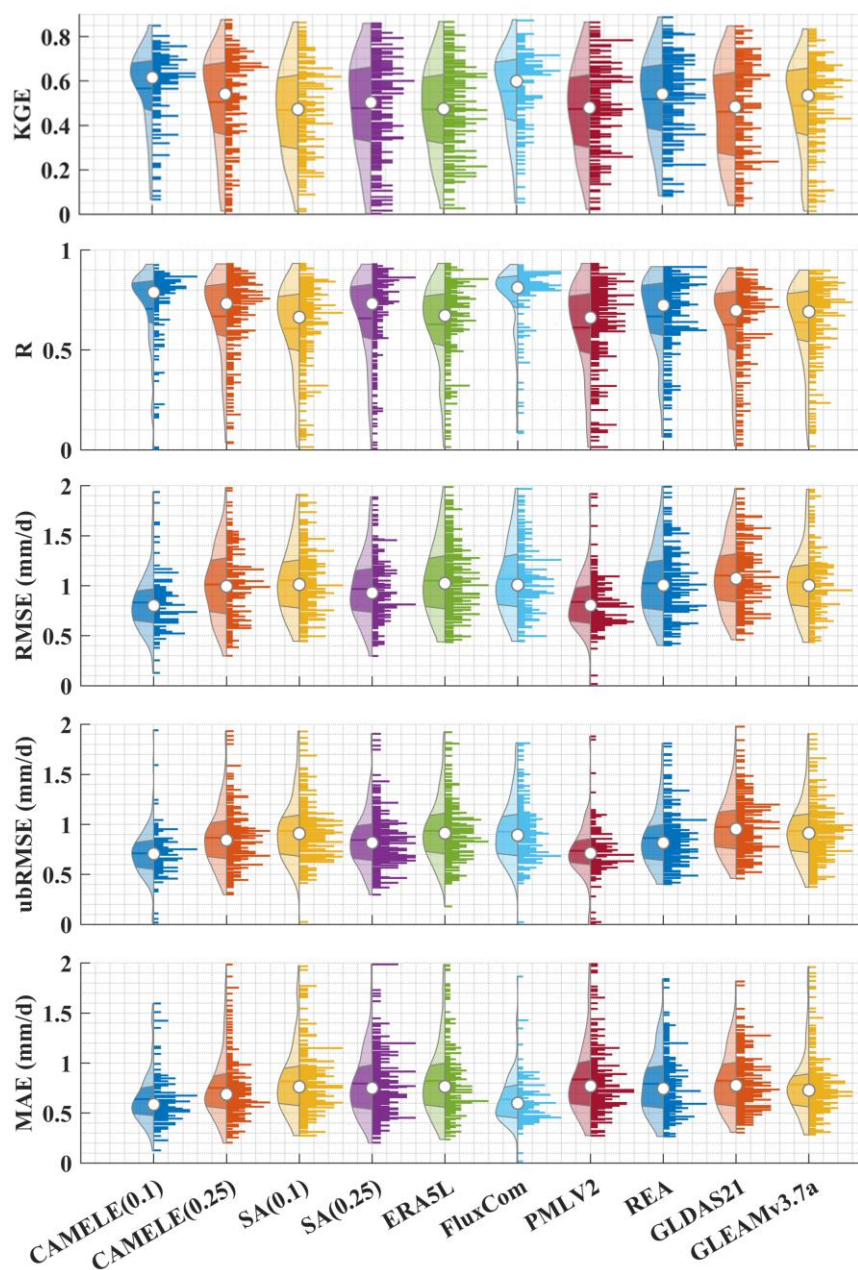


Figure 7 Violin plots obtained by aggregating five different statistical indicators, calculated separately for each site. In each violin plot, the left side represents the

distribution, with the shaded area indicating the box plot, the dot representing the mean, and the right side showing the histogram.

Table 4 Average values of indicators corresponding to different products, calculated based on the comprehensive results obtained for each site. The bolded sections indicate the schemes with the best performance in their respective metrics.

Product		RMSE (mm/d)	ubRMSE (mm/d)	MAE (mm/d)	KGE	R
0.1°-daily	CAMELE	0.83	0.71	0.64	0.57	0.71
	SA	1.05	0.93	0.82	0.47	0.61
	ERA5L	1.05	0.94	0.82	0.47	0.63
	FluxCom	1.07	0.93	0.64	0.55	0.74
	PMLv2	0.84	0.74	0.84	0.47	0.61
0.25°-daily	CAMELE	1.03	0.87	0.75	0.51	0.67
	SA	0.97	0.84	0.80	0.48	0.66
	REA	1.02	0.86	0.80	0.48	0.67
	GLDAS21	1.10	0.97	0.83	0.46	0.63
	GLEAMv3.7a	1.03	0.93	0.79	0.49	0.64

Table 4 presents the average values of different metrics in **Figure 7**, boldly highlighting the optimal products corresponding to each metric. It can be observed that CAMELE exhibits significant improvements in performance at a resolution of 0.1°, particularly in terms of the error metrics RMSE and ubRMSE, surpassing other products. This further confirms the effectiveness of our fusion scheme in reducing product errors. Additionally, although the performance of CAMELE at a resolution of 0.25° is comparable to other products, there is still a slight decline compared to its performance at 0.1°. This can be attributed partly to the inherent errors in the input products and partly to the decreasing representativeness of FluxNet, which serves as the reference at the 0.25° grid. Nevertheless, we can still consider CAMELE to have good accuracy.



Figure 8 Heatmaps of five statistical indicators, where each row corresponds to the mean value for all sites of the specific PFT, and each column corresponds to a product. The product with the best performance for that PFT is highlighted in bold within each row. (a)-(c) represent three error indicators: RMSE, ubRMSE, and MAE; (d)-(e) represent two goodness-of-fit indicators: KGE and R.

Table 5 Optimal product corresponding to different PFTs under various statistical indicators against observations from FluxNet sites

IGBP (n-sites)	RMSE (mm/d)	ubRMSE (mm/d)	MAE (mm/d)	KGE	R
<i>CRO</i> (20)	CAMELE	CAMELE	CAMELE	PMLv2	CAMELE

<i>CSH (3)</i>		PMLv2		FluxCom	FluxCom
<i>DBF (26)</i>		CAMELE		REA	
<i>DNF (1)</i>			FluxCom	CAMELE	
<i>EBF (15)</i>			CAMELE	GLEAM	
<i>ENF (49)</i>			FluxCom	CAMELE	
<i>GRA (39)</i>	PMLv2	CAMELE		CAMELE	CAMELE
<i>MF (9)</i>	CAMELE		CAMELE	REA	FluxCom
<i>OSH (13)</i>			FluxCom	CAMELE	
<i>SAV (9)</i>					
<i>SNO (1)</i>			CAMELE	REA	
<i>WET (21)</i>			PMLv2	FluxCom	
<i>WSA (6)</i>	CAMELE				

Furthermore, we classified 212 sites according to PFTs and analyzed the statistical indicators of different PFTs corresponding to each site. The results are represented in **Figure 8** as a heatmap, and the corresponding optimal products for other PFTs sites are marked in **Table 5**. The results show that CAMELE performs the best in almost all PFTs categories, as indicated by various indicators. While on sites where other products perform better, CAMELE's indicators are comparable to the optimal products, albeit slightly inferior. This indicates that our fusion approach effectively combines the advantages of different products, resulting in superior fusion results across different vegetation types.

From the results, it is evident that CAMELE performs well across various vegetation types. To delve deeper into the reasons behind this performance, we conduct site-scale analyses at two resolutions, evaluating errors and computed weights for different PFTs sites. These are visualized in radar chart format in **Figure 9**.

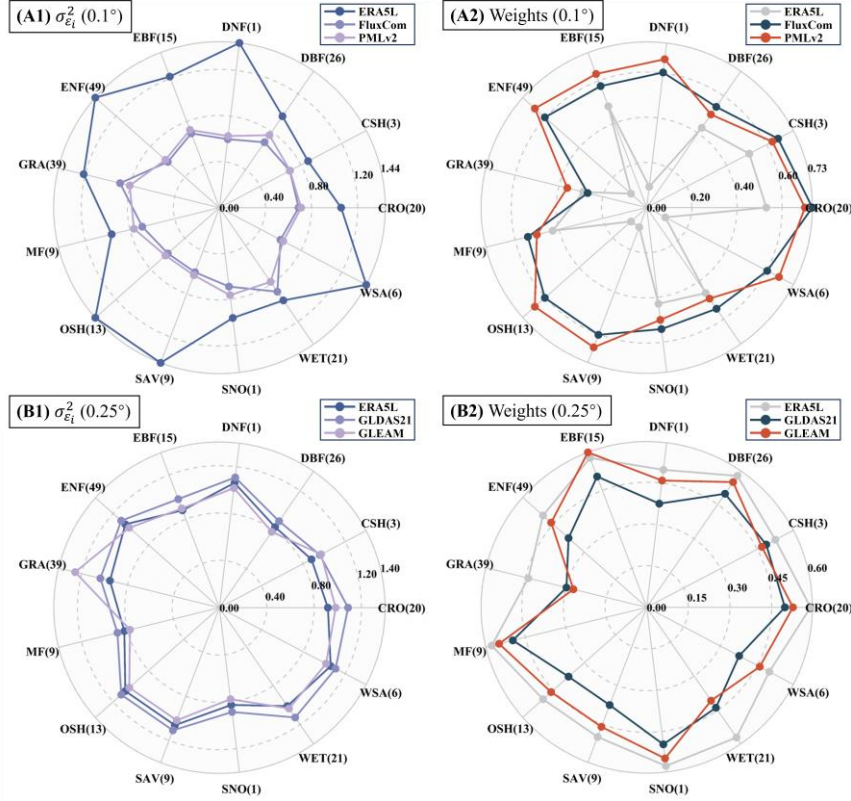


Figure 9 Mean collocation-based errors and weights of different products at various PFTs sites at (A) 0.1° and (B) 0.25° resolutions. The parentheses next to each PFTs name denote the corresponding number of sites.

The results from **Figure 9** demonstrate that the error-weighting calculation method based on collocation effectively considers the error situation of inputs, thereby providing reasonable weight assignments. At 0.1° resolution, ERA5L's error is significantly higher across all PFTs than FluxCom and PMLv2, resulting in relatively lower corresponding weights. FluxCom and PMLv2 exhibit closer performance, with higher weights at most PFT sites. At 0.25° resolution, ERA5L, GLDAS21, and GLEAM perform more evenly, with minimal differences, resulting in closer weights. The weights for different inputs vary noticeably with changes in PFTs, depending on the performance of other products within the same combination.

Products with more significant errors correspondingly have lower weights, affirming the rationale behind the fusion method. However, it is essential to note that the presented results depict the mean values of errors and weights across all sites; there might be variations among sites with the same PFTs.

In summary, using the filtered daily-scale data from 212 FluxNet sites as a reference, we conducted a benchmark analysis with CAMELE and demonstrated its good fit with the observed data. Additionally, by comparing the performance of different products at each site, we further illustrated that CAMELE exhibits similar or slightly improved accuracy and minor errors compared to existing products.

4.3. Assessment and comparison of multi-year average

In this section, we will first analyze and compare the performance of CAMELE with other products in estimating the multi-year mean and extreme values of ET at the site scale. Subsequently, a global-scale analysis will be conducted for the same periods (0.1°: 2001 to 2015; 0.25°: 2000 to 2017) to examine the distribution of multi-year daily average ET calculated by different products. For site comparisons, we have selected monthly mean ET values and three quantiles (5th, 50th, and 95th) to represent the products' performance in estimating ET's average and extreme values.

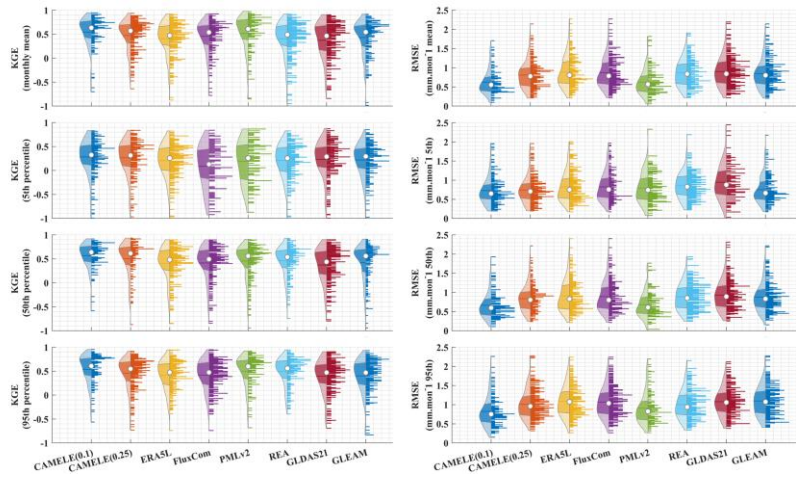


Figure 10 Violin plots depicting the KGE and RMSE metrics calculated for CAMELE and other products based on the monthly mean, 5th, 50th, and 95th percentiles at each FluxNet site. The left four columns represent KGE plots, while the right four columns represent RMSE plots. The dots in the violin plots represent the median, and the horizontal lines represent the mean.

Table 6 Average values of KGE and RMSE corresponding to different products, calculated based on the results obtained for each site. The bolded sections indicate the schemes with the best performance in their respective metrics.

Product		KGE			
		Mean	5 th	50 th	95 th
0.1°-daily	CAMELE	0.54	0.28	0.57	0.54
	ERA5L	0.41	0.21	0.40	0.42
	FluxCom	0.45	0.09	0.42	0.42
	PMLv2	0.52	0.19	0.46	0.50
0.25°-daily	CAMELE	0.47	0.26	0.50	0.45
	REA	0.40	0.21	0.46	0.50
	GLDAS21	0.37	0.23	0.37	0.40
	GLEAMv3.7a	0.43	0.22	0.42	0.40
Product		RMSE (mm/mon)			
		Mean	5 th	50 th	95 th
0.1°-daily	CAMELE	0.63	0.73	0.66	0.83

	ERA5L	0.89	0.83	0.91	1.09
	FluxCom	0.87	0.83	0.89	1.07
	PMLv2	0.63	0.80	0.68	0.91
	CAMELE	0.81	0.74	0.84	1.01
0.25°-daily	REA	0.86	0.85	0.88	1.01
	GLDAS21	0.90	0.95	0.93	1.08
	GLEAMv3.7a	0.85	0.75	0.88	1.10

The information in **Figure 10** corresponds to the data presented in **Table 6**, which involves the calculation of KGE and RMSE at each site, followed by statistical analysis. From the distribution of the violin plots, it can be observed that a violin plot with a closer belly to 1 indicates better results in terms of the KGE.

The results show that CAMELE outperforms other products in the estimation of monthly averages and the 5th, 50th, and 95th percentiles at both 0.1° and 0.25° resolutions. Its performance in capturing monthly averages is noteworthy, with a noticeable improvement in the KGE and RMSE metrics relative to the inputs. Examining the results for percentiles, CAMELE shows a relatively poorer estimation for shallow values (5th percentile) but still demonstrates some improvement compared to the input data, albeit influenced by input errors.

At 0.1°, PMLv2 and FluxCom perform just below the fusion result, aligning with the previous error and weight analysis. At 0.25°, GLEAM and REA closely follow CAMELE, with REA exhibiting slightly better estimation results for extremely high values (95th percentile) than CAMELE. Despite this, the analysis results still indicate that the products obtained reflect well the multi-year averages and extremes of ET, holding promise as reliable products for analyzing ET variations.

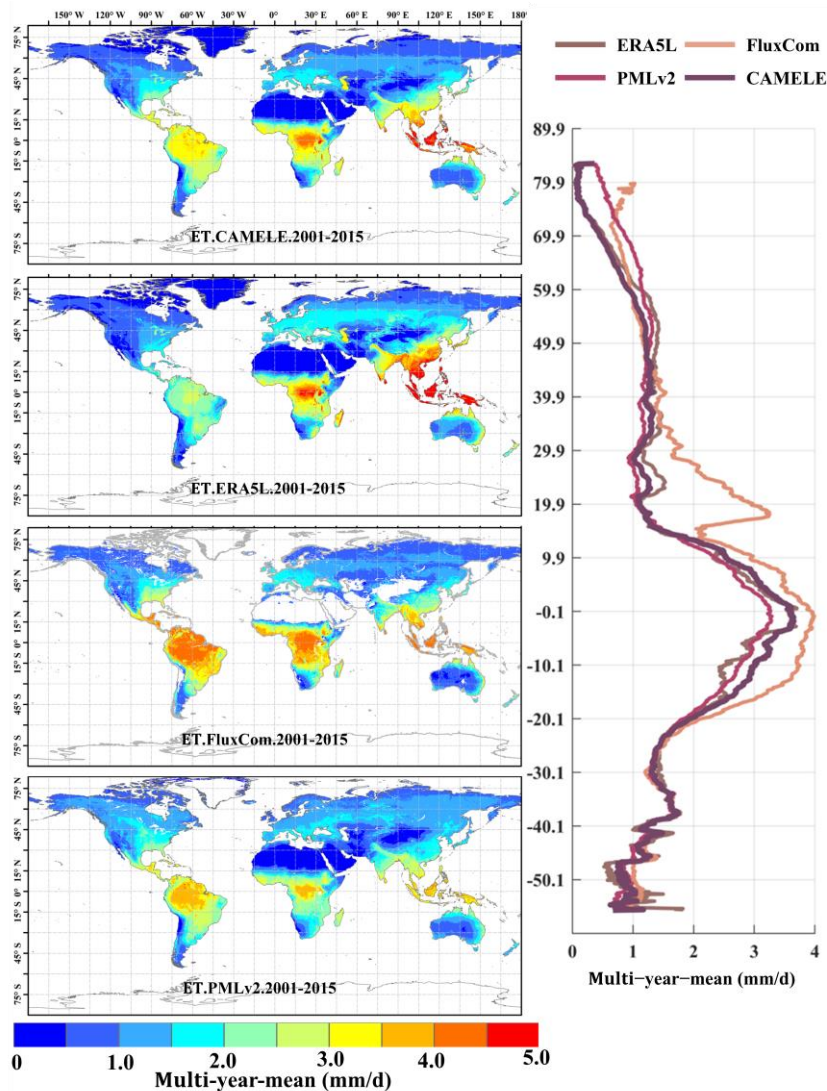


Figure 11 Global distribution of multi-year daily average ET at 0.1° for CAMELE, ERA5L, FluxCom, and PMLv2, depicted alongside corresponding variation curves of multi-year daily average ET with latitude. The results in **Figure 11** indicate significant differences in the multi-year daily average distribution of global evapotranspiration (ET) among different products. Specifically, ERA5L shows noticeably higher values in East Asia than other products,

while FluxCom and PMLv2 exhibit higher values in the Amazon rainforest and southern Africa regions. This distribution pattern is consistent with the error results obtained from the EIVD calculation, indicating that these products possess certain uncertainties in the regions. In terms of the latitudinal distribution pattern, except for FluxCom, which displays distinct fluctuations, the variability among the other products is relatively similar. This suggests that despite spatial differences among the different products, they maintain consistency in the overall quantity.

Figure 12 presents the results with a resolution of 0.25° . It can be observed that compared to the 0.1° distribution, the spatial distribution of annual average evapotranspiration (ET) is more consistent among different products at 0.25° , showing larger ET values in tropical regions. The main differences are concentrated in the Amazon rainforest and the Congo Basin, where GLEAM and GLDAS results are higher than REA's. The assigned weights for REA's inputs (MERRA2, GLDAS, and GLEAM.) are approximately equal in these two regions, each contributing about one-third to the overall calculation (Lu et al., 2021). This balanced allocation results in the REA being distributed among them roughly equally over multiple years in these two regions. The latitude variation plots show that the results from each product are very close, providing additional evidence for the reliability of CAMELE.

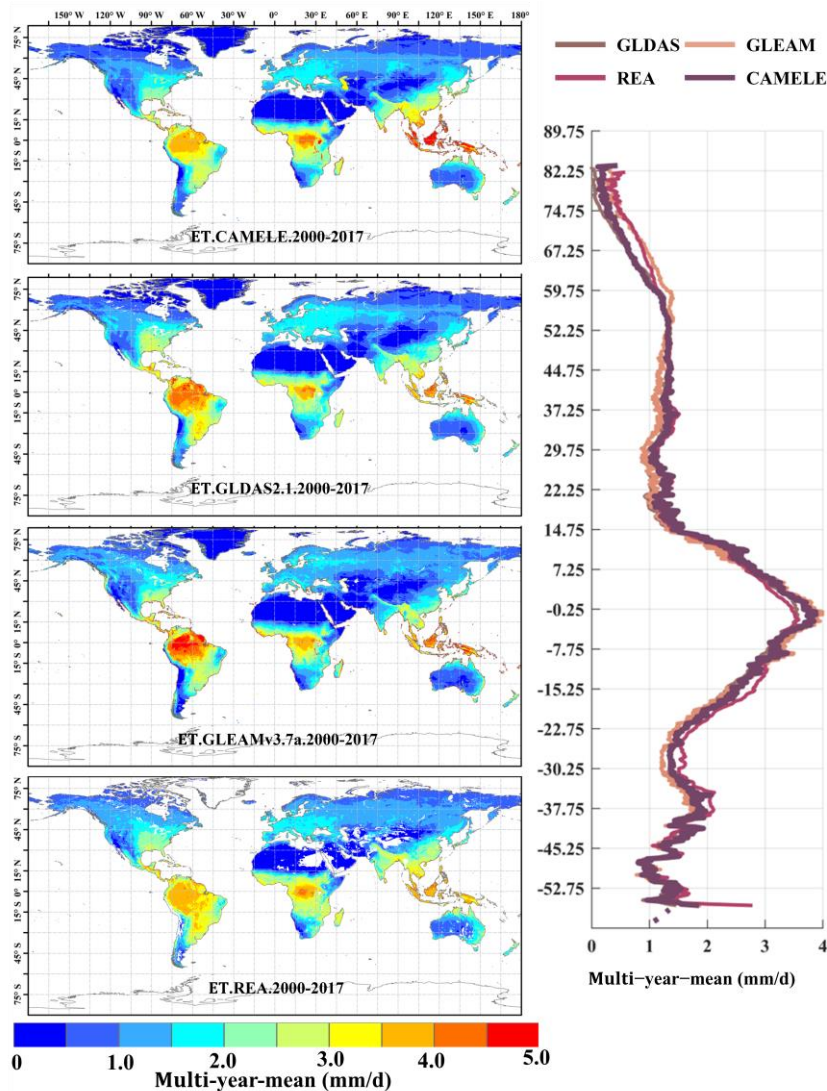


Figure 12 Global distribution of multi-year daily average ET at 0.25° for CAMELE, GLDAS2.1, GLEAMv3.7a, and REA, depicted alongside corresponding variation curves of multi-year daily average ET with latitude.

In parallel, it is worth noting that, despite the regional disparities that may arise when contrasting the trends by CAMELE with inputs, a noteworthy consistency emerges when examining these trends along latitudinal gradients. This notable alignment

signifies the robustness of CAMELE to some extent. It underscores the capacity of CAMELE to capture ET patterns, providing further insights for the scientific community.

4.4. Assessment and comparison of linear trend and seasonality

In this section, we first validate and compare the performance of CAMELE with other products in estimating multi-year trends and seasonality at the site scale. Due to the inconsistent time lengths of FluxNet sites, trends at many sites are not significant. Therefore, we deliberately selected 13 sites with continuous evapotranspiration (ET) observations for the same 11-year period (2004 to 2014) and with significant trends. The annual ET values for each year were calculated as the mean of the 13 sites for that year, allowing the computation of linear trends and seasonality. We employed singular spectrum analysis (SSA), which assumes an additive decomposition $A = LT + ST + R$. In this decomposition, LT represents the long-term trend in the data, ST is the seasonal or oscillatory trend (or trends), and R is the remainder.

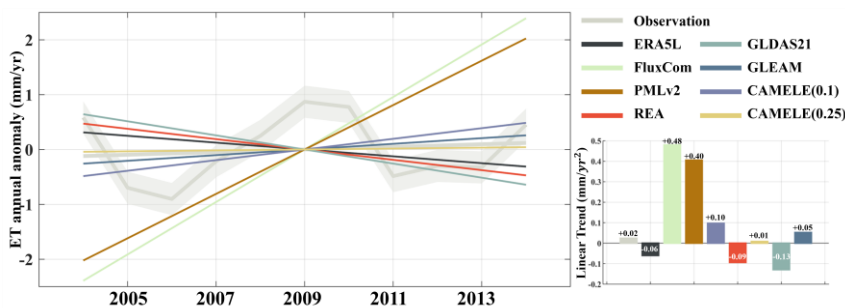


Figure 13 Comparison of linear trend from 2004 to 2014 among 13 FluxNet sites using CAMELE and other products. The trends have been subjected to SSA decomposition, removing seasonality. The gray enveloping line represents the mean plus the standard deviation of the 13 sites.

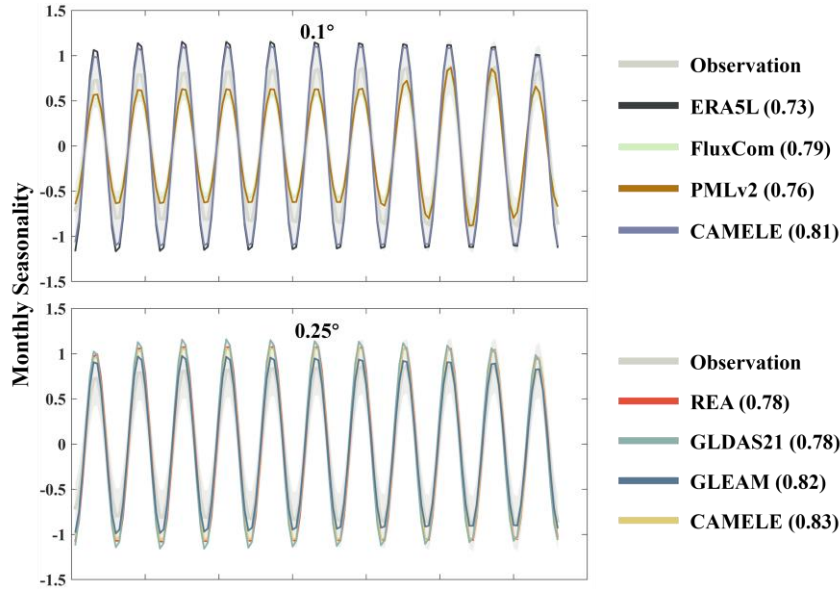


Figure 14 Comparison of seasonal variations from 2004 to 2014 among 13 FluxNet sites using CAMELE and other products. The seasonality has been obtained through SSA decomposition, with the gray area representing the observed values. The parentheses in each product name indicate the KGE coefficient comparing with the observed values.

In **Figure 13** and **Figure 14**, based on observations from FluxNet sites, we analyzed the performance of CAMELE and other products in estimating the linear trend and seasonality of ET over multiple years. It is important to note that we only present the analysis results for 13 sites with continuous 11-year observations, and the performance of different ET products in trend estimation at individual sites still varies, not fully reflecting the overall performance on all grids in terms of trend and seasonality. Nevertheless, such a comparison can still provide valuable insights. Examining the results of the linear trend, both PMLv2 and FluxCom exhibit a significant upward trend, well above the observations. On the contrary, ERA5L, GLDAS, and REA show a noticeable downward trend, while CAMELE demonstrates a gradual upward trend closer to the observations. Additionally, GLEAM slightly

outperforming CAMELE at a resolution of 0.25°. Overall, CAMELE shows good agreement with site observations in capturing the multi-year linear trend of ET.

Table 7

Continuing with the analysis of seasonality, the KGE index comparing each product's results with observed values is provided in parentheses next to the product name. Generally, all products exhibit a good representation of ET's seasonal variations. CAMELE's 0.1° seasonal results closely match FluxCom (with the two lines almost overlapping). However, the fluctuations it reflects are higher than the observed values. This is likely due to keeping the 8-day average results of FluxCom consistent with PMLv2 every 8 days, and the variability in ET primarily originates from ERA5L results. This aspect may need improvement in subsequent research. At 0.25°, CAMELE's seasonal representation is closer to the observed results. The differences in CAMELE's performance at the two resolutions are mainly attributed to input variations, which we discuss in the following section as potential areas for improvement.

Table 7 Comparison of CAMELE results at 13 continuous 10-year observational sites:

(a) Comparison of Linear trend; (b) KGE values for monthly seasonality.

Site Name	(a) Linear Trend (mm/yr) (2004-2014)		(b) KGE of seasonality		
	Observation	CAMELE (0.1)	CAMELE (0.25)	CAMELE (0.1)	CAMELE (0.25)
BE Lon	0.15	0.06	0.05	0.65	0.71
CH Lae	-0.33	-0.36	-0.35	0.80	0.80
CH Oe2	0.25	0.37	0.67	0.85	0.49
CZ BK1	-0.44	-0.53	-0.66	0.54	0.71
DE Gri	0.11	0.03	0.24	0.61	0.54
DE Kli	0.68	0.77	0.85	0.78	0.52
FR Gri	0.41	0.36	0.55	0.71	0.55
GF Guy	-0.47	-0.50	-0.45	0.77	0.73
IT BCi	0.21	0.25	0.28	0.61	0.56
IT Noe	0.11	0.02	0.04	0.61	0.51
US GLE	-0.14	-0.17	-0.01	0.64	0.49

设置了格式: 字体: 加粗

设置了格式: 字体: 加粗

设置了格式: 字体: 加粗

格式化表格

设置了格式: 字体: 非加粗

设置了格式: 字体: 非加粗

<u>US SRM</u>	<u>-0.42</u>	<u>-0.45</u>	<u>-0.63</u>	<u>0.52</u>	<u>0.61</u>
<u>ZM Mon</u>	<u>0.16</u>	<u>0.22</u>	<u>0.09</u>	<u>0.56</u>	<u>0.51</u>

设置了格式: 字体: 非倾斜

Furthermore, we present the linear trend estimated by CAMELE from 2004 to 2014 at 13 sites, along with the KGE values for monthly seasonality. The results indicate that regardless of the resolution, whether 0.1° or 0.25°, the trends estimated by CAMELE are consistent with the observed trends, with minor difference. In comparison to the observed monthly seasonality, the KGE values exceed 0.5 at all sites, with some sites exceeding 0.7, indicating that CAMELE can effectively capture the seasonal variations.

The results indicate that CAMELE effectively captures the multi-year changes in ET, but at 0.1°, it tends to overestimate seasonal fluctuations. We further generated global maps of multi-year linear trends in ET, estimating trends using Theil–Sen's slope method and testing significance with the Mann–Kendall method. The dotted areas indicate trends passing a significance test at a 5% level.

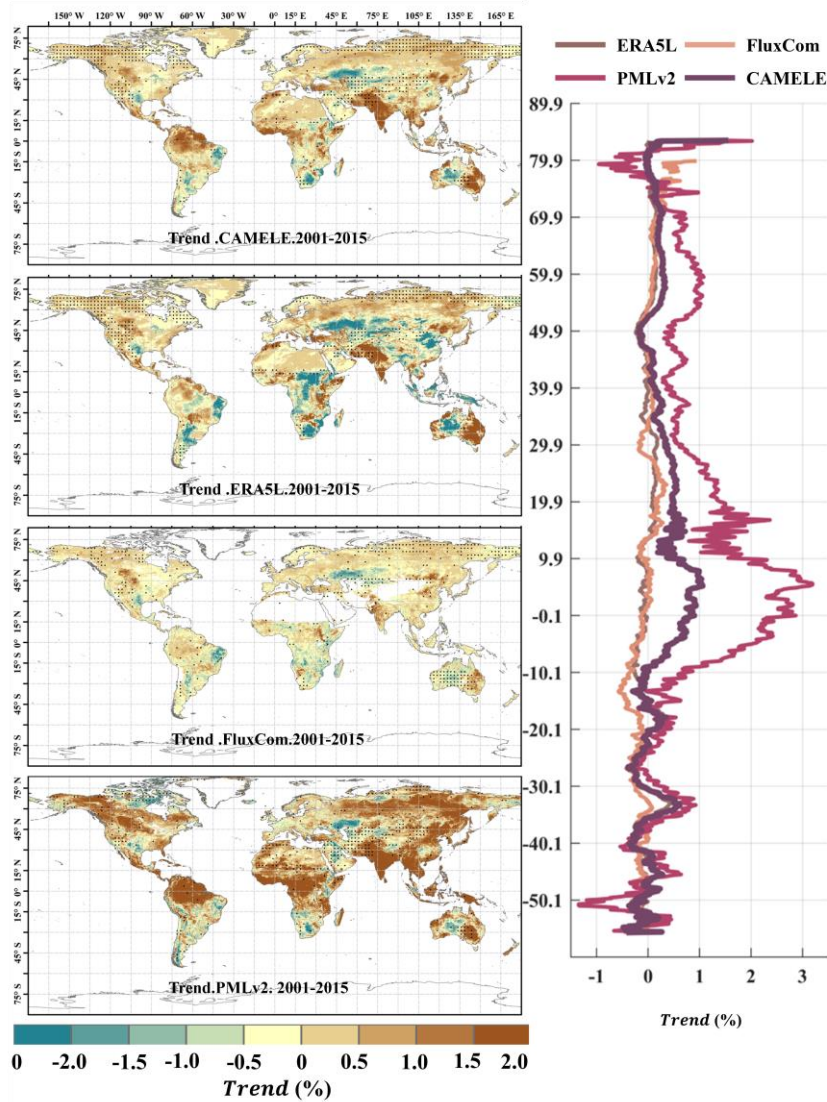


Figure 15 Global distribution of multi-year linear trend at 0.1° for CAMELE, ERA5L, FluxCom, and PMLv2, depicted alongside corresponding average trend with latitude. The trend is estimated with Theil–Sen’s slope method, and the significance level is tested with the Mann–Kendall method. The dotted area indicates that the trend has passed the significance test at 5 % level.

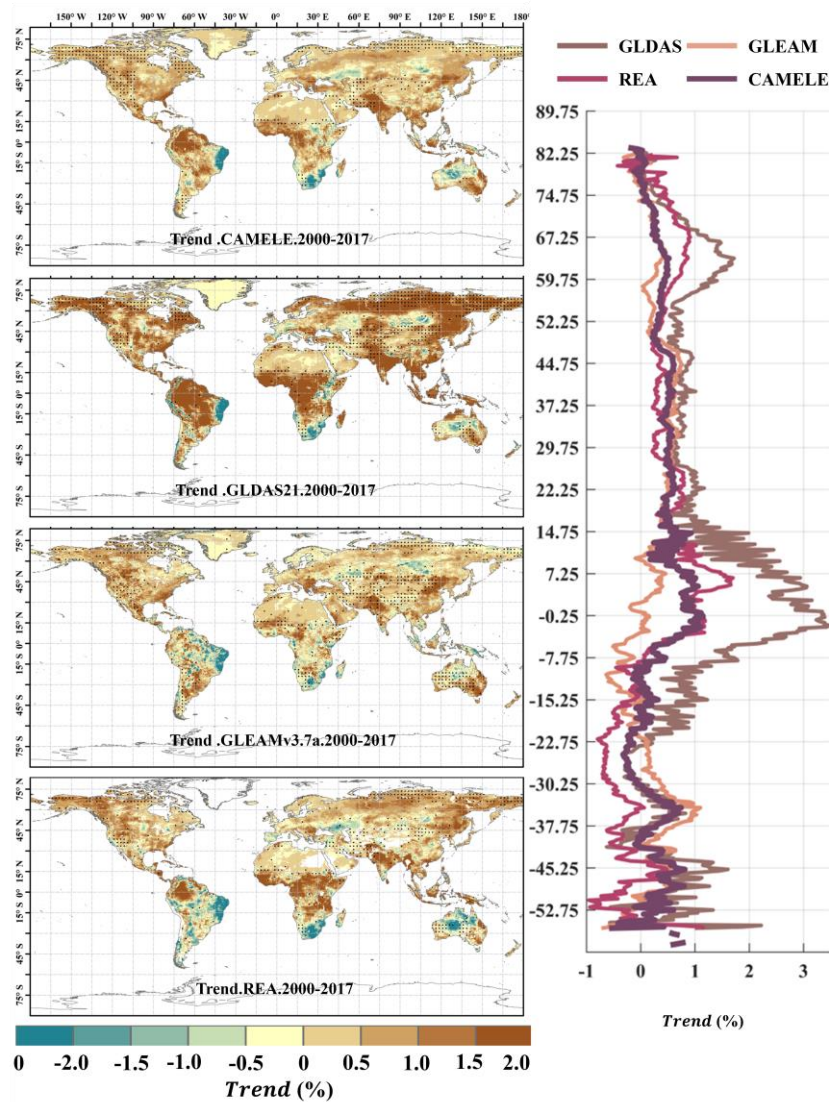


Figure 16 Global distribution of multi-year linear trend at 0.25° for CAMELE, GLDAS2.1, GLEAMv3.7a, and REA, depicted alongside corresponding average trend with latitude. The trend is estimated with Theil–Sen’s slope method, and the significance level is tested with the Mann–Kendall method. The dotted area indicates that the trend has passed the significance test at 5 % level.

Figure 15 ~~Figure 15 错误!未找到引用源。~~ and **Figure 16** ~~Figure 16 错误!未找到引用源。~~ present the linear trends of multi-year daily scale evapotranspiration (ET) calculated for different products at resolutions of 0.1° and 0.25°, respectively. The corresponding latitude-dependent variations of the rate of change are shown on the right side. It can be observed that the differences in linear trends among the different products are more significant than the multi-year averages, and in some regions, they even exhibit opposite trends. For example, at 0.1° resolution, PMLv2 shows a global increase of 1.0% in ET in most regions, while the results from CAMELE, ERA5L, and PMLv2 indicate a milder increase in ET in the Amazon rainforest, southern Africa, and northwestern Australia. At 0.25° resolution, except for GLDAS2.1, which shows an apparent global increase in ET, the results from CAMELE, GLEAMv3.7a, and REA indicate milder variations in global ET.

5. Discussion

5.1. Impact of underlying assumptions in collocation analysis

The collocation analysis system relies on key assumptions, including linearity (linear regression model), stationarity (unchanged probability distribution over time), error orthogonality (independence between random error and true signal), and zero error cross-correlation (independence between random errors). Potential error autocorrelation is considered with lag-1 [day] series. Various studies have examined the validity and impact of these assumptions. Numerous studies have examined the validity of these assumptions and their impact on the outcomes if violated (Tsamalis, 2022; Duan et al., 2021; Gruber et al., 2020).

The linearity assumption shapes the error model by including additive and multiplicative biases and zero-mean random error. Although some studies have explored the application of a nonlinear rescaling technique (Yilmaz and Crow, 2013; Zwieback et al., 2016), those efforts are primarily limited to soil moisture signals and

901 often fail to accurately represent the true signal unless all datasets share a similar
 902 signal-to-noise ratio (SNR). However, it is worth noting that after rescaling processes,
 903 such as cumulative distribution function (CDF) matching or climatology removal, the
 904 resulting time series (anomalies) are often considered linearly related to the truth since
 905 higher-order error terms are removed. In addition, multiplicative relationships have
 906 been more commonly identified in rainfall products (Li et al., 2018). In contrast,
 907 collocation analysis within the context of ET products frequently suggests that linear
 908 relationships are reasonable (Li et al., 2022; Park et al., 2023). Therefore, the linear
 909 error model remains a robust implementation, though it has the potential for
 910 improvement through rescaling techniques.

911 Regarding violating the stationarity assumption, the evapotranspiration signal does
 912 not strictly adhere to this characteristic. However, by collocating triplets with similar
 913 magnitude variations, the influence of this violation is minimized. Nonetheless,
 914 disparities in climatology between datasets can still arise for various reasons (Su and
 915 Ryu, 2015). Several proposed alternatives aim to address this issue, such as removing
 916 the climatology of inputs (Stoffelen, 1998; Yilmaz and Crow, 2014; Draper et al.,
 917 2013) and subsequently analyzing the random error variance of the anomalies (Dong
 918 et al., 2020b). Nevertheless, obtaining a reliable estimation of climatology proves
 919 challenging in practice.

920 The assumption of error orthogonality assumes independence between random error
 921 and true signal, i.e., $\sigma_{\varepsilon_i\theta} = 0$. A few studies have examined this assumption. Yilmaz
 922 and Crow (2014) investigated such violations using four in situ sites and concluded
 923 that the impact is negligible since rescaling mitigates or compensates for bias.
 924 Additionally, non-orthogonality results in non-zero error cross-correlation (ECC),
 925 although the latter is considered more important. Vogelzang et al. (2022) also
 926 investigated this violation recently and demonstrated minimal second-order impact.

927 Non-zero ECC conditions introduce more substantial bias in the results compared to
 928 other violations mainly due to two reasons: (1) they cannot be mitigated by rescaling;

929 (2) they cannot be compensated even with equal magnitude for all inputs; and (3) they
930 have been frequently reported in recent studies for various variables (Li et al., 2018,
931 2022; Gruber et al., 2016b). Gruber et al. (2016a) proposed the extended collocation
932 method, which effectively addresses the ECC of selected pairs. Moreover, the EIVD
933 method adopts the error cross-correlation framework. In the following section, we
934 will analyze the ECC between pairs.

935 **5.2. Analysis of error cross-correlation**

936 This study assumes non-zero ECC (Error-Correction Coefficient) conditions exist
937 between FluxCom and PMLv2 at 0.1° and between ERA5L and GLEAM at 0.25° .
938 However, non-zero ECC conditions were also possible between other pairs. Therefore,
939 we presented the EIVD-based ECC results of various pairs.

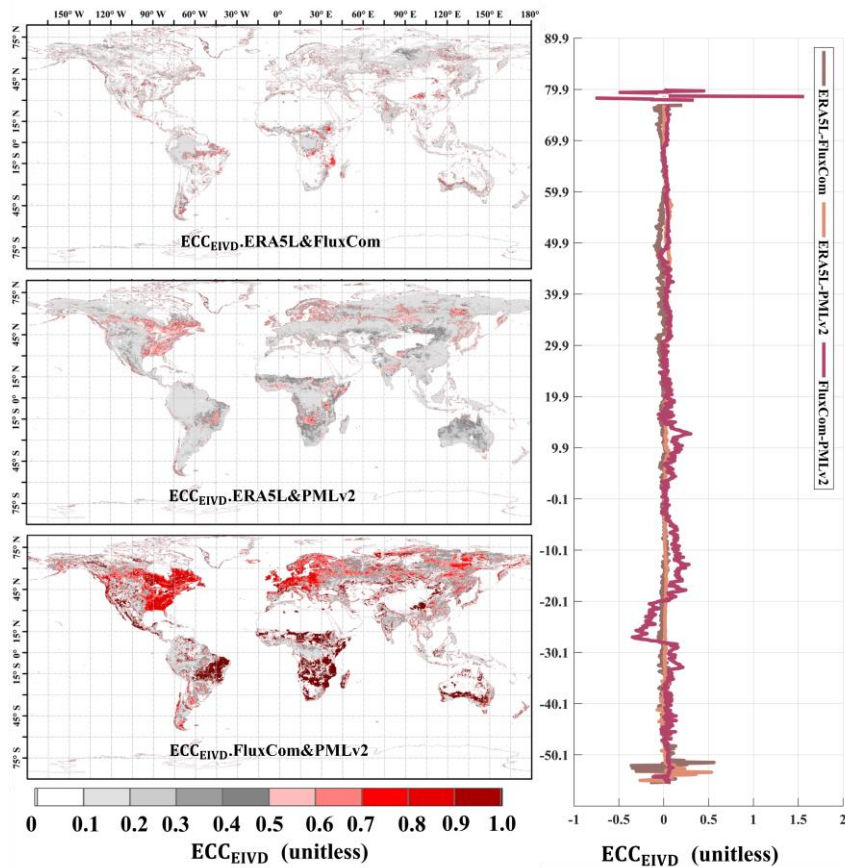


Figure 17 Global Distribution of estimated error cross-correlation (ECC) between ERA5L, FluxCom, and PMLv2 pairwise using EIVD alongside relevant variation curves of average with latitude.

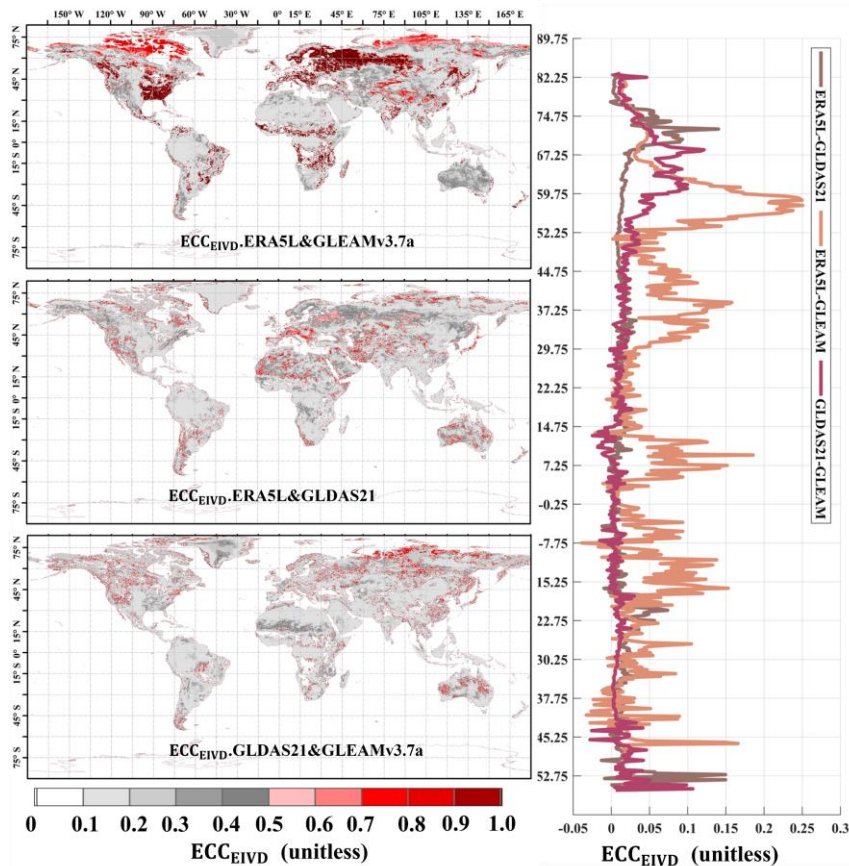


Figure 18 Global Distribution of estimated error cross-correlation (ECC) between ERA5L, GLEAMv3.7a, and GLDAS21 pairwise using EIVD alongside relevant variation curves of average with latitude.

As depicted in [Figure 17](#) and [Figure 18](#), at a resolution of 0.1° , the ECC values of FluxCom and PMLv2 were notably higher than those of ERA5L-FluxCom and ERA5L-PMLv2. The global average ECC value for FluxCom-PMLv2 was 0.16, and regions with high ECC values were identified in the eastern United States, most of Europe, and the western Amazon, areas densely covered by measurement sites. Since both FluxCom and PMLv2 incorporated corrections based on FluxNet measurement sites, there is likely some overlap between the sites used by

both products in the high ECC regions. This partially explains the shared source of random errors between the two datasets.

The global error correlations of GLEAM-GLDAS and ERA5L-GLDAS are relatively low. The random error of ERA5L correlates with that of GLEAM, primarily in arid regions such as the Sahara Desert, Northwest China, and central Australia, where the average ECC exceeds 0.20. The global average ECC of ERA5L-GLEAM is approximately 0.14. A higher error correlation is observed for ERA5L-GLEAM, with a mean ECC value of 0.26, which is expected since meteorological information from ECMWF is reanalyzed for both datasets. However, ECC values for GLEAM-GLDAS and ERA5L-GLDAS are generally low globally, supporting the assumption of zero ECC for these two pairs.

Our findings highlight the significant impact of Error Cross Correlation (ECC) between FluxCom-PMLv2 and ERA5L-GLEAM at 0.1° and 0.25° resolutions, respectively. Mathematically, when a triplet exhibits a high ECC value (>0.3) between two sets, it indicates a preference for the remaining independent product as the "better" one, potentially leading to an underestimation of its error variance. However, it is essential to note that the overall ECC values for other pairs are relatively small, suggesting that the zero ECC assumptions can be considered valid for these pairs across most areas. Therefore, these assumptions are unlikely to affect the relevant results of uncertainties significantly. Nevertheless, we have considered the non-zero ECC condition between FluxCom-PMLv2 and ERA5L-GLEAM in this study, as it requires careful consideration.

5.3. Comparison of different fusion schemes

In this section, we conducted comparisons in three aspects: (1) comparing the performance of CAMELE at different resolutions; (2) comparing the performance of different change fusion schemes, explicitly changing the input products' versions (GLDAS21 to GLDAS20 or GLDAS22, GLEAMv3.7a to v3.7b); and (3) comparing

the performance of the results obtained without considering the ECC impact.

We conducted a comprehensive comparison of our fusion approach with several alternative schemes. Specifically, these schemes encompassed utilizing only ERA5L and PMLV2 at 0.1° based on the IVD method (Comb1), changing the versions of GLDAS2 and GLEAM at 0.25° based on the EIVD method (Comb2-5), and two TC fusion approaches at 0.1° and 0.25°, which did not incorporate ECC.

It should be noted that the Comb2 scheme, which includes GLDAS20, covers the period from 1980 to 2014, while the other 0.25° comparison schemes (Comb3-5) span from 2003 to 2022. The combinations based on TC (assuming zero ECC) had the same inputs as CAMELE at both resolutions.

Table 87 Average metrics for CAMELE and other fusion schemes at all sites. The bolded sections indicate the schemes with the best performance in their respective metrics.

Product	RMSE (mm/d)	ubRMSE (mm/d)	MAE (mm/d)	KGE	R
CAMELE (0.1)	0.83	0.71	0.64	0.57	0.71
CAMELE (0.25)	1.03	0.87	0.75	0.51	0.67
ERA5L+PMLV2 (Comb1-0.1 / IVD)	1.13	1.00	0.89	0.46	0.61
ERA5L+GLDAS20+GLEAMv3.7a (Comb2-0.25 / EIVD)	1.09	0.89	0.87	0.44	0.66
ERA5L+GLDAS22+GLEAMv3.7a (Comb3-0.25 / EIVD)	1.20	0.95	0.94	0.44	0.68
ERA5L+GLDAS22+GLEAMv3.7b (Comb4-0.25 / EIVD)	1.19	0.94	0.93	0.44	0.69
ERA5L+GLDAS21+GLEAMv3.7b (Comb5-0.25 / EIVD)	1.05	0.90	0.80	0.49	0.69
ERA5L+FluxCom+PMLv2 (Zero-ECC-0.1 / TC)	1.06	0.91	0.80	0.46	0.60
ERA5L+GLDAS21+GLEAMv3.7a (Zero-ECC-0.25 / TC)	1.26	1.03	0.99	0.39	0.61

According to the information in the table, CAMELE (0.1°) results were superior in all indicators. Firstly, when comparing the performance of CAMELE at resolutions of 0.1° and 0.25°, it was observed that the fused product performed slightly worse at the 0.25° resolution. Additionally, the representative of FluxNet sites at the 0.25° resolution decreased, leading to degraded statistical indicators.

At the 0.1° resolution, we conducted a comparison of results obtained by exclusively fusing ERA5-Land and PMLv2. Multiple indicators indicated that this approach did not enhance the accuracy of ET estimates and fell significantly short of the scheme employed in CAMELE. This implies that using only two product sets as input did not allow for effective error analysis through collocation analysis, resulting in suboptimal fusion results. More importantly, the limitation of employing only two datasets prevented us from effectively acquiring error information through collocation analysis (Dong et al., 2020a, 2019). Consequently, we made the strategic decision to ensure the inclusion of three datasets as inputs, facilitating the utilization of the EIVD method and maintaining methodological consistency between the 0.1° and 0.25° resolutions.

Furthermore, when comparing the results of different fusion schemes between CAMELE and Comb2-5 at the 0.25° resolution, CAMELE performed better regarding error metrics (RMSE, ubRMSE, MAE). The differences in fitting metrics (KGE, R) were insignificant, indicating that the choice of fusion scheme primarily affected the errors of the fusion results. The relatively poorer performance of other fusion schemes could be due to the lack of consideration for non-zero ECC. For example, non-zero ECC between GLDAS-2.2 and ERA5L has been reported in a recent study (Li et al., 2023a).

For the comparative analysis of the GLDAS2.0 and GLDAS2.1 schemes, the usage of GLDAS2.1 yielded better performance. The GLDAS-2.1 simulation leverages conditions from the GLDAS-2.0 simulation, with improved models driven by a combination of datasets. Previous research has demonstrated that GLDAS-2.1 offers improvements in the regional-scale simulation of hydrological variables compared to GLDAS-2.0 (Qi et al., 2018, 2020). Consequently, we chose to incorporate GLDAS-2.1 data for as much of the time series as possible.

Moreover, when comparing the fusion effects with and without considering non-zero ECC conditions, it was evident that considering ECC information could effectively

improve the performance of the fused product, which further demonstrated the reliability and advantages of the fusion method employed in this study.

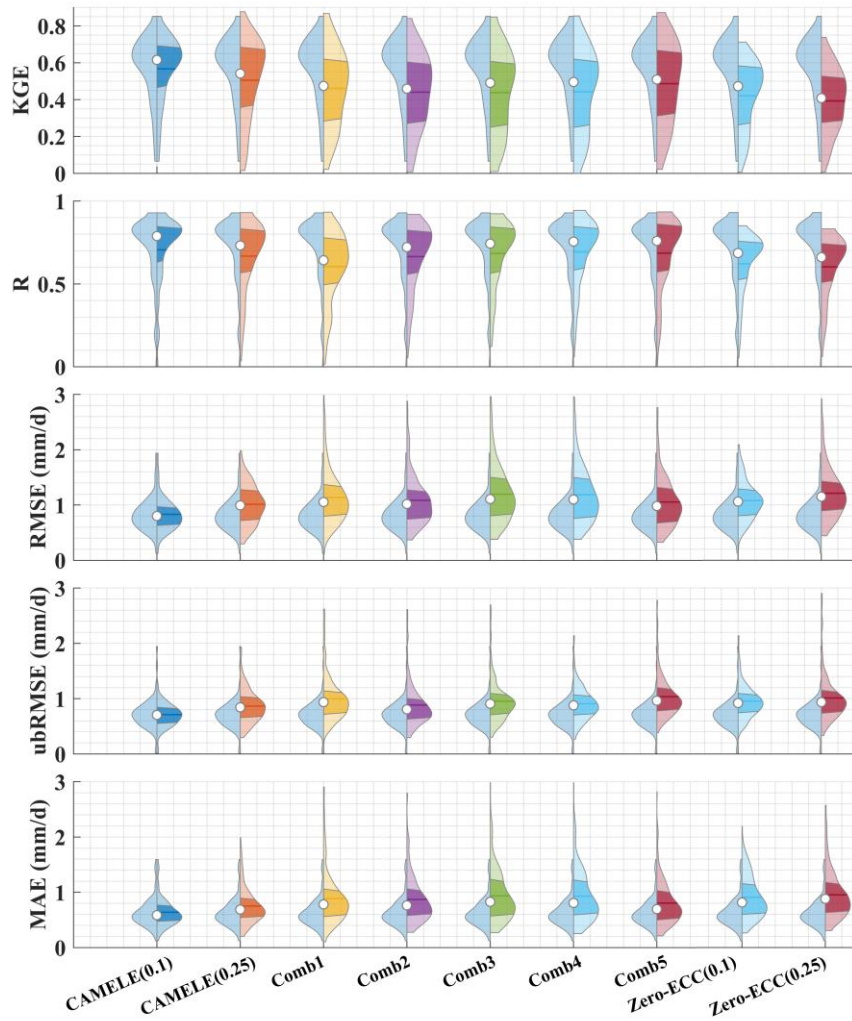


Figure 19 Violin plot comparing KGE, R, RMSE, ubRMSE and MAE of CAMELE with other fusion schemes. The right half of each violin plot represents the distribution, with shaded areas indicating the box plot, where the horizontal line corresponds to the median and the dot represents the mean. The left half represents the results of CAMELE (0.1°) for comparison.

We further provided violin plots for different metrics, comparing the results of each fusion scheme to CAMELE (0.1°) as shown in [Figure 19](#)~~Figure 19~~. The results indicated that the fusion schemes adopted were significantly superior to other schemes based on the distribution of results for all metrics across all sites. Regarding KGE and R, CAMELE's results were concentrated near 1 for most sites. Regarding RMSE, ubRMSE, and MAE, their results were concentrated below one mm/d. The results in the plots also suggested that CAMELE performed slightly worse at 0.25° compared to 0.1° but still outperformed other combination results. Additionally, comparing CAMELE and the zero-ECC scheme in the plots further highlighted the importance of considering non-zero ECC conditions.

5.4. Potential Applications and Future Enhancements

In this section, we delve into the potential applications of our product and outline our commitment to future enhancements to maintain its accuracy and relevance.

Here, we identify three potential applications for our transpiration product: (1) Global ET Trends: Our product facilitates global-scale analysis of current ET patterns and long-term trends, essential for comprehending ecosystem responses to evolving environmental conditions in a warming climate; (2) Transpiration-to-Evapotranspiration Ratio: Our merging approach can fuse multi-source global gridded transpiration data, allowing for the examination of the transpiration-to-evapotranspiration ratio. This analysis can enhance water resource management and water availability predictions in diverse regions; (3) Attribution analysis: Our product is a valuable tool for attribution analysis, helping researchers identify the drivers of patterns. This knowledge is crucial for understanding the roles of climate variability, land-use changes, and other factors in shaping terrestrial water fluxes.

Furthermore, we are committed to enhancing our product proactively. Key strategies include: (1) Data Update and Validation: To ensure our product's continued accuracy and reliability, we will prioritize regularly updating the data used in this study to the

latest versions. By adopting this approach, we aim to provide users with results that reflect the latest advancements in scientific knowledge; (2) Enhanced Integration and Error Reduction: We continually refine estimates by incorporating additional data sources and implementing extended collocation method to minimize errors; (3) Integration of High-Resolution Regional ET Data: Recognizing the significance of regional-scale insights, we will focus on improving the accuracy of CAMELE by integrating higher-resolution regional ET data. This integration will enable more precise regional estimation.

In summary, these endeavors collectively represent our commitment to maintaining our product's quality and relevance, ensuring its value for the scientific community.

6. Conclusion

This study used a collocation-based approach for merging data considering non-zero conditions. We successfully generated a long-term daily CAMELE evapotranspiration (ET) product at resolutions of 0.1° (2000 to 2020) and 0.25° (1980 to 2022) by integrating five widely used datasets: ERA5L, FluxCom, PMLv2, GLDAS, and GLEAM. The key findings of our study are as follows:

1. Collocation analysis methods proved to be a reliable tool for evaluating ET products without a reference dataset. This approach shows promising potential for error characterization, especially in regions with limited data availability or on a global scale. The evaluation results provided valuable insights into the data merging process.
2. Compared to five input products, REA, and simple average, the CAMELE product performed well when evaluated against FluxNet flux tower data. While CAMELE may not excel in all individual metrics, it effectively reduces errors associated with the input products. The result showed Pearson correlation coefficients (R) of 0.63 and 0.65, root-mean-square errors (RMSE) of 0.81 and 0.73 mm/d, unbiased root-mean-square errors (ubRMSE) of 1.20 and 1.04 mm/d, mean absolute errors

(MAE) of 0.81 and 0.73 mm/d, and Kling-Gupta efficiency (KGE) of 0.60 and 0.65 on average over resolutions of 0.1° and 0.25°, respectively. This robust performance is especially evident when assessing its comprehensive station-scale evaluation.

3. For different plant functional types (PFTs), the CAMELE product outperformed the five input products, REA, and simple average in most PFTs. Although FluxCom and PMLv2 performed slightly better than CAMELE at some PFT sites, considering that both utilized FluxNet sites for product calibration, it indirectly demonstrates the promising and robust performance of CAMELE.

4. Based on site-scale observations, CAMELE effectively captures the multi-year linear trend of ET. The accuracy of the multi-year mean value depicted by CAMELE is improved compared to the input data. Moreover, it accurately characterizes extreme ET values. However, there is a slight overestimation in representing the seasonality, which needs further improvement in future research.

5. When utilizing the error information derived from collocation analysis for merging, it is crucial to consider the potential presence of non-zero error compensation conditions (ECC). Comparing the merging schemes with and without considering non-zero ECC, it was found that considering ECC improves the accuracy of the merging process. Additionally, when using collocation analysis, it is necessary to identify which products may have ECC in advance, providing more effective support for data merging and obtaining more accurate product error information.

In conclusion, our proposed collocation-based data merging approach demonstrates the promising potential for merging ET products. The resulting CAMELE product exhibited good overall performance at site-based and regional scales, meeting the requirements for more detailed research. Furthermore, further evaluation of the merged product in specific regions is necessary to improve its accuracy. In future studies, dynamic weights could be computed by considering suitable merging periods

1119 for different products to enhance the quality of the merged product, and more
1120 sophisticated combination schemes could be explored to improve accuracy.

1121 **Author Contribution**

1122 C.L. conceived and designed the study, collected and analyzed the data, and wrote the
1123 manuscript. H.Y participated in the study design, provided intellectual insights, and
1124 reviewed the manuscript for important intellectual content. Z.L. and W.Y provided
1125 substantial input in the study design and data interpretation and revised the manuscript.
1126 Z.T., J.H., and S.L. guided the research process and critically reviewed the manuscript.
1127 All authors have read and approved the final version of the manuscript.

1128 **Competing interests**

1129 The authors declare that they have no conflict of interest.

1130 **Acknowledgments**

1131 This research was supported by the China National Key R&D Program (grant no.
1132 2022YFC3002802), the National Natural Science Foundation of China (grant nos.
1133 51979140, 52309022 and 42041004), and the Key Research and Development
1134 Program of Yunnan Province, China (grant no. 202203AA080010).

1135 **Data and code availability**

1136 The datasets utilized in this research can be accessed through the links provided in the
1137 Dataset Section. The CAMELE products are available via
1138 <https://doi.org/10.5281/zenodo.5704736> (Li et al., 2023b). The data is distributed
1139 under a Creative Commons Attribution 4.0 License. Additionally, we provide
1140 example MATLAB codes to read and plot CAMELE data and employ IVD and EIVD
1141 methods to merge the inputs. Please refer to the latest version., 202306.

1143 **Reference**

- 1144 Baker, J. C. A., Garcia-Carreras, L., Gloor, M., Marsham, J. H., Buermann, W., da
1145 Rocha, H. R., Nobre, A. D., de Araujo, A. C., and Spracklen, D. V.:
1146 Evapotranspiration in the Amazon: spatial patterns, seasonality, and recent trends in
1147 observations, reanalysis, and climate models, *Hydrology and Earth System Sciences*,
1148 25, 2279–2300, <https://doi.org/10.5194/hess-25-2279-2021>, 2021.
- 1149 Barraza Bernadas, V., Grings, F., Restrepo-Coupe, N., and Huete, A.: Comparison of
1150 the performance of latent heat flux products over southern hemisphere forest
1151 ecosystems: estimating latent heat flux error structure using in situ measurements and
1152 the triple collocation method, *International Journal of Remote Sensing*, 39, 6300–
1153 6315, 2018.
- 1154 Bates, J. M. and Granger, C. W.: The combination of forecasts, *Journal of the*
1155 *Operational Research Society*, 20, 451–468, 1969.
- 1156 Chen, Z., Zhu, Z., Jiang, H., and Sun, S.: Estimating daily reference
1157 evapotranspiration based on limited meteorological data using deep learning and
1158 classical machine learning methods, *Journal of Hydrology*, 591,
1159 <https://doi.org/10.1016/j.jhydrol.2020.125286>, 2020.
- 1160 De Lannoy, G. J., Houser, P. R., Verhoest, N. E., Pauwels, V. R., and Gish, T. J.:
1161 Upscaling of point soil moisture measurements to field averages at the OPE3 test site,
1162 *Journal of Hydrology*, 343, 1–11, 2007.
- 1163 Deng, X., Zhu, L., Wang, H., Zhang, X., Tong, C., Li, S., and Wang, K.: Triple
1164 Collocation Analysis and In Situ Validation of the CYGNSS Soil Moisture Product,
1165 *IEEE Journal of Selected Topics in Applied Earth Observations and Remote Sensing*,
1166 16, 1883–1899, <https://doi.org/10.1109/jstars.2023.3235111>, 2023.
- 1167 Dong, J. and Crow, W. T.: An Improved Triple Collocation Analysis Algorithm for
1168 Decomposing Autocorrelated and White Soil Moisture Retrieval Errors, *Journal of*
1169 *Geophysical Research: Atmospheres*, 122, 13,081–13,094,
1170 <https://doi.org/10.1002/2017jd027387>, 2017.
- 1171 Dong, J., Crow, W. T., Duan, Z., Wei, L., and Lu, Y.: A double instrumental variable
1172 method for geophysical product error estimation, *Remote Sensing of Environment*,
1173 225, 217–228, <https://doi.org/10.1016/j.rse.2019.03.003>, 2019.
- 1174 Dong, J., Wei, L., Chen, X., Duan, Z., and Lu, Y.: An instrument variable based
1175 algorithm for estimating cross-correlated hydrological remote sensing errors, *Journal*
1176 *of Hydrology*, 581, 124413, <https://doi.org/10.1016/j.jhydrol.2019.124413>, 2020a.

1177 Dong, J., Lei, F., and Wei, L.: Triple Collocation Based Multi-Source Precipitation
 1178 Merging, *Frontiers in Water*, 2, <https://doi.org/10.3389/frwa.2020.00001>, 2020b.

1179 Dong, J., Crow, W. T., Chen, X., Tangdamrongsub, N., Gao, M., Sun, S., Qiu, J., Wei,
 1180 L., Gao, H., and Duan, Z.: Statistical uncertainty analysis-based precipitation merging
 1181 (SUPER): A new framework for improved global precipitation estimation, *Remote
 1182 Sensing of Environment*, 283, 113299, <https://doi.org/10.1016/j.rse.2022.113299>,
 1183 2022.

1184 Draper, C., Reichle, R., de Jeu, R., Naeimi, V., Parinussa, R., and Wagner, W.:
 1185 Estimating root mean square errors in remotely sensed soil moisture over continental
 1186 scale domains, *Remote Sensing of Environment*, 137, 288–298, 2013.

1187 Duan, Z., Duggan, E., Chen, C., Gao, H., Dong, J., and Liu, J.: Comparison of
 1188 traditional method and triple collocation analysis for evaluation of multiple gridded
 1189 precipitation products across Germany, *Journal of Hydrometeorology*,
 1190 <https://doi.org/10.1175/JHM-D-21-0049.1>, 2021.

1191 ECMWF, S. P.: In IFS documentation CY40R1 Part IV: Physical Processes, ECMWF:
 1192 Reading, UK, 111–113, 2014.

1193 Ershadi, A., McCabe, M. F., Evans, J. P., Chaney, N. W., and Wood, E. F.: Multi-site
 1194 evaluation of terrestrial evaporation models using FLUXNET data, *Agricultural and
 1195 Forest Meteorology*, 187, 46–61, <https://doi.org/10.1016/j.agrformet.2013.11.008>,
 1196 2014.

1197 Feng, Y., Cui, N., Zhao, L., Hu, X., and Gong, D.: Comparison of ELM, GANN,
 1198 WNN and empirical models for estimating reference evapotranspiration in humid
 1199 region of Southwest China, *Journal of Hydrology*, 536, 376–383,
 1200 <https://doi.org/10.1016/j.jhydrol.2016.02.053>, 2016.

1201 Gan, R., Zhang, Y., Shi, H., Yang, Y., Eamus, D., Cheng, L., Chiew, F. H., and Yu,
 1202 Q.: Use of satellite leaf area index estimating evapotranspiration and gross
 1203 assimilation for Australian ecosystems, *Ecohydrology*, 11, e1974, 2018.

1204 Gentine, P., Massmann, A., Lintner, B. R., Hamed Alemohammad, S., Fu, R., Green,
 1205 J. K., Kennedy, D., and Vilà-Guerau de Arellano, J.: Land–atmosphere interactions in
 1206 the tropics – a review, *Hydrology and Earth System Sciences*, 23, 4171–4197,
 1207 <https://doi.org/10.5194/hess-23-4171-2019>, 2019.

1208 Gruber, A., Su, C., Crow, W. T., Zwieback, S., Dorigo, W., and Wagner, W.:
 1209 Estimating error cross-correlations in soil moisture data sets using extended
 1210 collocation analysis, *Journal of Geophysical Research: Atmospheres*, 121, 1208–1219,
 1211 2016a.

1212 Gruber, A., Su, C.-H., Zwieback, S., Crow, W., Dorigo, W., and Wagner, W.: Recent
1213 advances in (soil moisture) triple collocation analysis, *International Journal of*
1214 *Applied Earth Observation and Geoinformation*, 45, 200–211,
1215 <https://doi.org/10.1016/j.jag.2015.09.002>, 2016b.

1216 Gruber, A., Dorigo, W. A., Crow, W., and Wagner, W.: Triple Collocation-Based
1217 Merging of Satellite Soil Moisture Retrievals, *IEEE Trans. Geosci. Remote Sensing*,
1218 55, 6780–6792, <https://doi.org/10.1109/TGRS.2017.2734070>, 2017.

1219 Gruber, A., Scanlon, T., van der Schalie, R., Wagner, W., and Dorigo, W.: Evolution
1220 of the ESA CCI Soil Moisture climate data records and their underlying merging
1221 methodology, *Earth System Science Data*, 11, 717–739, [https://doi.org/10.5194/essd-](https://doi.org/10.5194/essd-11-717-2019)
1222 11-717-2019, 2019.

1223 Gruber, A., De Lannoy, G., Albergel, C., Al-Yaari, A., Brocca, L., Calvet, J. C.,
1224 Colliander, A., Cosh, M., Crow, W., Dorigo, W., Draper, C., Hirschi, M., Kerr, Y.,
1225 Konings, A., Lahoz, W., McColl, K., Montzka, C., Muñoz-Sabater, J., Peng, J.,
1226 Reichle, R., Richaume, P., Rüdiger, C., Scanlon, T., van der Schalie, R., Wigneron, J.
1227 P., and Wagner, W.: Validation practices for satellite soil moisture retrievals: What
1228 are (the) errors?, *Remote Sensing of Environment*, 244, 111806,
1229 <https://doi.org/10.1016/j.rse.2020.111806>, 2020.

1230 Gupta, H. V., Kling, H., Yilmaz, K. K., and Martinez, G. F.: Decomposition of the
1231 mean squared error and NSE performance criteria: Implications for improving
1232 hydrological modelling, *Journal of hydrology*, 377, 80–91, 2009.

1233 Han, S. and Tian, F.: A review of the complementary principle of evaporation: from
1234 the original linear relationship to generalized nonlinear functions, *Hydrology and*
1235 *Earth System Sciences*, 24, 2269–2285, <https://doi.org/10.5194/hess-24-2269-2020>,
1236 2020.

1237 Hao, Y., Baik, J., and Choi, M.: Combining generalized complementary relationship
1238 models with the Bayesian Model Averaging method to estimate actual
1239 evapotranspiration over China, *Agricultural and Forest Meteorology*, 279, 107759,
1240 <https://doi.org/10.1016/j.agrformet.2019.107759>, 2019.

1241 Hersbach, H., Bell, B., Berrisford, P., Hirahara, S., Horányi, A., Muñoz-Sabater, J.,
1242 Nicolas, J., Peubey, C., Radu, R., Schepers, D., Simmons, A., Soci, C., Abdalla, S.,
1243 Abellan, X., Balsamo, G., Bechtold, P., Biavati, G., Bidlot, J., Bonavita, M., Chiara,
1244 G., Dahlgren, P., Dee, D., Diamantakis, M., Dragani, R., Flemming, J., Forbes, R.,
1245 Fuentes, M., Geer, A., Haimberger, L., Healy, S., Hogan, R. J., Hólm, E., Janisková,
1246 M., Keeley, S., Laloyaux, P., Lopez, P., Lupu, C., Radnoti, G., Rosnay, P., Rozum, I.,
1247 Vamborg, F., Villaume, S., and Thépaut, J.: The ERA5 global reanalysis, *Quarterly*
1248 *Journal of the Royal Meteorological Society*, 146, 1999–2049,

1249 <https://doi.org/10.1002/qj.3803>, 2020.

1250 Hoareau, N., Portabella, M., Lin, W., Ballabrera-Poy, J., and Turiel, A.: Error
 1251 characterization of sea surface salinity products using triple collocation analysis,
 1252 IEEE Transactions on Geoscience and Remote Sensing, 56, 5160–5168, 2018.

1253 Jia, Y., Li, C., Yang, H., Yang, W., and Liu, Z.: Assessments of three
 1254 evapotranspiration products over China using extended triple collocation and water
 1255 balance methods, Journal of Hydrology, 614, 128594, 2022.

1256 Jiang, C. and Ryu, Y.: Multi-scale evaluation of global gross primary productivity and
 1257 evapotranspiration products derived from Breathing Earth System Simulator (BESS),
 1258 Remote Sensing of Environment, 186, 528–547, 2016.

1259 Jiang, C., Ryu, Y., Fang, H., Myneni, R., Claverie, M., and Zhu, Z.: Inconsistencies of
 1260 interannual variability and trends in long-term satellite leaf area index products, Glob
 1261 Chang Biol, 23, 4133–4146, <https://doi.org/10.1111/gcb.13787>, 2017.

1262 Jiang, C., Guan, K., Pan, M., Ryu, Y., Peng, B., and Wang, S.: BESS-STAIR: a
 1263 framework to estimate daily, 30 m, and all-weather crop evapotranspiration using
 1264 multi-source satellite data for the US Corn Belt, Hydrology and Earth System
 1265 Sciences, 24, 1251–1273, <https://doi.org/10.5194/hess-24-1251-2020>, 2020.

1266 Jiménez, C., Prigent, C., Mueller, B., Seneviratne, S. I., McCabe, M. F., Wood, E. F.,
 1267 Rossow, W. B., Balsamo, G., Betts, A. K., Dirmeyer, P. A., Fisher, J. B., Jung, M.,
 1268 Kanamitsu, M., Reichle, R. H., Reichstein, M., Rodell, M., Sheffield, J., Tu, K., and
 1269 Wang, K.: Global intercomparison of 12 land surface heat flux estimates, Journal of
 1270 Geophysical Research, 116, <https://doi.org/10.1029/2010jd014545>, 2011.

1271 Jung, M., Koirala, S., Weber, U., Ichii, K., Gans, F., Camps-Valls, G., Papale, D.,
 1272 Schwalm, C., Tramontana, G., and Reichstein, M.: The FLUXCOM ensemble of
 1273 global land-atmosphere energy fluxes, Sci Data, 6, 74,
 1274 <https://doi.org/10.1038/s41597-019-0076-8>, 2019.

1275 Khan, M. S., Liaqat, U. W., Baik, J., and Choi, M.: Stand-alone uncertainty
 1276 characterization of GLEAM, GLDAS and MOD16 evapotranspiration products using
 1277 an extended triple collocation approach, Agricultural and Forest Meteorology, 252,
 1278 256–268, <https://doi.org/10.1016/j.agrformet.2018.01.022>, 2018.

1279 Kim, S., Pham, H. T., Liu, Y. Y., Marshall, L., and Sharma, A.: Improving the
 1280 Combination of Satellite Soil Moisture Data Sets by Considering Error Cross
 1281 Correlation: A Comparison Between Triple Collocation (TC) and Extended Double
 1282 Instrumental Variable (EIVD) Alternatives, IEEE Transactions on Geoscience and
 1283 Remote Sensing, 59, 7285–7295, <https://doi.org/10.1109/tgrs.2020.3032418>, 2021a.

1284 Kim, S., Sharma, A., Liu, Y. Y., and Young, S. I.: Rethinking satellite data merging:
1285 from averaging to SNR optimization, *IEEE Transactions on Geoscience and Remote*
1286 *Sensing*, 60, 1–15, 2021b.

1287 Kling, H., Fuchs, M., and Paulin, M.: Runoff conditions in the upper Danube basin
1288 under an ensemble of climate change scenarios, *Journal of Hydrology*, 424–425, 264–
1289 277, <https://doi.org/10.1016/j.jhydrol.2012.01.011>, 2012.

1290 Knoben, W. J. M., Freer, J. E., and Woods, R. A.: Technical note: Inherent
1291 benchmark or not? Comparing Nash–Sutcliffe and Kling–Gupta efficiency scores,
1292 *Hydrology and Earth System Sciences*, 23, 4323–4331, [https://doi.org/10.5194/hess-](https://doi.org/10.5194/hess-23-4323-2019)
1293 23-4323-2019, 2019.

1294 Koster, R. D., Liu, Q., Reichle, R. H., and Huffman, G. J.: Improved Estimates of
1295 Pentad Precipitation Through the Merging of Independent Precipitation Data Sets,
1296 *Water Resources Research*, 57, <https://doi.org/10.1029/2021wr030330>, 2021.

1297 Leuning, R., Zhang, Y., Rajaud, A., Cleugh, H., and Tu, K.: A simple surface
1298 conductance model to estimate regional evaporation using MODIS leaf area index and
1299 the Penman-Monteith equation, *Water Resources Research*, 44, 2008.

1300 Leuning, R., Zhang, Y. Q., Rajaud, A., Cleugh, H., and Tu, K.: Correction to “A
1301 simple surface conductance model to estimate regional evaporation using MODIS leaf
1302 area index and the Penman-Monteith equation,” *Water Resources Research*, 45,
1303 <https://doi.org/10.1029/2008wr007631>, 2009.

1304 Li, B., Rodell, M., Kumar, S., Beaudoin, H. K., Getirana, A., Zaitchik, B. F.,
1305 Goncalves, L. G., Cossetin, C., Bhanja, S., Mukherjee, A., Tian, S., Tangdamrongsub,
1306 N., Long, D., Nanteza, J., Lee, J., Policelli, F., Goni, I. B., Daira, D., Bila, M., Lannoy,
1307 G., Mocko, D., Steele-Dunne, S. C., Save, H., and Bettadpur, S.: Global GRACE Data
1308 Assimilation for Groundwater and Drought Monitoring: Advances and Challenges,
1309 *Water Resour. Res.*, 55, 7564–7586, <https://doi.org/10.1029/2018WR024618>, 2019a.

1310 Li, C., Tang, G., and Hong, Y.: Cross-evaluation of ground-based, multi-satellite and
1311 reanalysis precipitation products: Applicability of the Triple Collocation method
1312 across Mainland China, *Journal of Hydrology*, 562, 71–83,
1313 <https://doi.org/10.1016/j.jhydrol.2018.04.039>, 2018.

1314 Li, C., Yang, H., Yang, W., Liu, Z., Jia, Y., Li, S., and Yang, D.: Error
1315 Characterization of Global Land Evapotranspiration Products: Collocation-based
1316 approach, *Journal of Hydrology*, 128102, 2022.

1317 Li, C., Liu, Z., Tu, Z., Shen, J., He, Y., and Yang, H.: Assessment of global gridded
1318 transpiration products using the extended instrumental variable technique (EIVD),
1319 *Journal of Hydrology*, 623, 129880, <https://doi.org/10.1016/j.jhydrol.2023.129880>,

1320 2023a.

1321 Li, C., Liu, Z., Yang, W., Tu, Z., Han, J., Sien, L., and Hanbo, Y.: CAMELE:
 1322 Collocation-Analyzed Multi-source Ensembled Land Evapotranspiration Data, ,
 1323 <https://doi.org/10.5281/zenodo.8047038>, 2023b.

1324 Li, X., Gentine, P., Lin, C., Zhou, S., Sun, Z., Zheng, Y., Liu, J., and Zheng, C.: A
 1325 simple and objective method to partition evapotranspiration into transpiration and
 1326 evaporation at eddy-covariance sites, *Agricultural and Forest Meteorology*, 265, 171–
 1327 182, <https://doi.org/10.1016/j.agrformet.2018.11.017>, 2019b.

1328 Li, X., Zhang, W., Vermeulen, A., Dong, J., and Duan, Z.: Triple collocation-based
 1329 merging of multi-source gridded evapotranspiration data in the Nordic Region,
 1330 *Agricultural and Forest Meteorology*, 335, 109451,
 1331 <https://doi.org/10.1016/j.agrformet.2023.109451>, 2023c.

1332 Lian, X., Piao, S., Huntingford, C., Li, Y., Zeng, Z., Wang, X., Ciais, P., McVicar, T.
 1333 R., Peng, S., Ottlé, C., Yang, H., Yang, Y., Zhang, Y., and Wang, T.: Partitioning
 1334 global land evapotranspiration using CMIP5 models constrained by observations,
 1335 *Nature Clim Change*, 8, 640–646, <https://doi.org/10.1038/s41558-018-0207-9>, 2018.

1336 Lin, C., Gentine, P., Huang, Y., Guan, K., Kimm, H., and Zhou, S.: Diel ecosystem
 1337 conductance response to vapor pressure deficit is suboptimal and independent of soil
 1338 moisture, *Agricultural and Forest Meteorology*, 250, 24–34, 2018.

1339 Loveland, T. R., Zhu, Z., Ohlen, D. O., Brown, J. F., Reed, B. C., and Yang, L.: An
 1340 analysis of the IGBP global land-cover characterization process, *Photogrammetric
 1341 engineering and remote sensing*, 65, 1021–1032, 1999.

1342 Lu, J., Wang, G., Chen, T., Li, S., Hagan, D. F. T., Kattel, G., Peng, J., Jiang, T., and
 1343 Su, B.: A harmonized global land evaporation dataset from model-based products
 1344 covering 1980–2017, *Earth System Science Data*, 13, 5879–5898,
 1345 <https://doi.org/10.5194/essd-13-5879-2021>, 2021.

1346 Ma, N., Szilagyi, J., and Jozsa, J.: Benchmarking large-scale evapotranspiration
 1347 estimates: A perspective from a calibration-free complementary relationship approach
 1348 and FLUXCOM, *Journal of Hydrology*, 590,
 1349 <https://doi.org/10.1016/j.jhydrol.2020.125221>, 2020.

1350 Majozi, N. P., Mannaerts, C. M., Ramoelo, A., Mathieu, R., Nickless, A., and Verhoef,
 1351 W.: Analysing surface energy balance closure and partitioning over a semi-arid
 1352 savanna FLUXNET site in Skukuza, Kruger National Park, South Africa, *Hydrology
 1353 and Earth System Sciences*, 21, 3401–3415, [https://doi.org/10.5194/hess-21-3401-
 1354 2017](https://doi.org/10.5194/hess-21-3401-2017), 2017.

1355 Martens, B., Miralles, D. G., Lievens, H., van der Schalie, R., de Jeu, R. A. M.,
1356 Fernández-Prieto, D., Beck, H. E., Dorigo, W. A., and Verhoest, N. E. C.:
1357 GLEAM v3: satellite-based land evaporation and root-zone soil moisture,
1358 Geoscientific Model Development, 10, 1903–1925, [https://doi.org/10.5194/gmd-10-](https://doi.org/10.5194/gmd-10-1903-2017)
1359 1903-2017, 2017.

1360 McColl, K. A., Vogelzang, J., Konings, A. G., Entekhabi, D., Piles, M., and Stoffelen,
1361 A.: Extended triple collocation: Estimating errors and correlation coefficients with
1362 respect to an unknown target, Geophysical Research Letters, 41, 6229–6236,
1363 <https://doi.org/10.1002/2014gl061322>, 2014.

1364 Ming, W., Ji, X., Zhang, M., Li, Y., Liu, C., Wang, Y., and Li, J.: A Hybrid Triple
1365 Collocation-Deep Learning Approach for Improving Soil Moisture Estimation from
1366 Satellite and Model-Based Data, Remote Sensing, 14,
1367 <https://doi.org/10.3390/rs14071744>, 2022.

1368 Miralles, D., De Jeu, R., Gash, J., Holmes, T., and Dolman, A.: Magnitude and
1369 variability of land evaporation and its components at the global scale, Hydrology and
1370 Earth System Sciences, 15, 967–981, 2011.

1371 Miralles, D. G., Gentile, P., Seneviratne, S. I., and Teuling, A. J.: Land-atmospheric
1372 feedbacks during droughts and heatwaves: state of the science and current challenges,
1373 Ann N Y Acad Sci, 1436, 19–35, <https://doi.org/10.1111/nyas.13912>, 2019.

1374 Mu, Q., Zhao, M., and Running, S. W.: Improvements to a MODIS global terrestrial
1375 evapotranspiration algorithm, Remote sensing of environment, 115, 1781–1800, 2011.

1376 Muñoz-Sabater, J., Dutra, E., Agustí-Panareda, A., Albergel, C., Arduini, G., Balsamo,
1377 G., Boussetta, S., Choulga, M., Harrigan, S., Hersbach, H., Martens, B., Miralles, D.
1378 G., Piles, M., Rodríguez-Fernández, N. J., Zsoter, E., Buontempo, C., and Thépaut, J.-
1379 N.: ERA5-Land: a state-of-the-art global reanalysis dataset for land applications,
1380 Earth Syst. Sci. Data, 13, 4349–4383, <https://doi.org/10.5194/essd-13-4349-2021>,
1381 2021.

1382 Pan, S., Pan, N., Tian, H., Friedlingstein, P., Sitch, S., Shi, H., Arora, V. K., Haverd,
1383 V., Jain, A. K., Kato, E., Lienert, S., Lombardozzi, D., Nabel, J. E. M. S., Ottlé, C.,
1384 Poulter, B., Zaehle, S., and Running, S. W.: Evaluation of global terrestrial
1385 evapotranspiration using state-of-the-art approaches in remote sensing, machine
1386 learning and land surface modeling, Hydrology and Earth System Sciences, 24, 1485–
1387 1509, <https://doi.org/10.5194/hess-24-1485-2020>, 2020.

1388 Park, J., Baik, J., and Choi, M.: Triple collocation-based multi-source evaporation and
1389 transpiration merging, Agricultural and Forest Meteorology, 331, 109353, 2023.

1390 Pastorello, G., Trotta, C., Canfora, E., Chu, H., Christianson, D., Cheah, Y. W.,

1391 Poindexter, C., Chen, J., Elbashandy, A., Humphrey, M., Isaac, P., Polidori, D.,
1392 Reichstein, M., Ribeca, A., van Ingen, C., Vuichard, N., Zhang, L., Amiro, B.,
1393 Ammann, C., Arain, M. A., Ardo, J., Arkebauer, T., Arndt, S. K., Arriga, N., Aubinet,
1394 M., Aurela, M., Baldocchi, D., Barr, A., Beamesderfer, E., Marchesini, L. B.,
1395 Bergeron, O., Beringer, J., Bernhofer, C., Berveiller, D., Billesbach, D., Black, T. A.,
1396 Blanken, P. D., Bohrer, G., Boike, J., Bolstad, P. V., Bonal, D., Bonnefond, J. M.,
1397 Bowling, D. R., Bracho, R., Brodeur, J., Brummer, C., Buchmann, N., Burban, B.,
1398 Burns, S. P., Buysse, P., Cale, P., Cavagna, M., Cellier, P., Chen, S., Chini, I.,
1399 Christensen, T. R., Cleverly, J., Collalti, A., Consalvo, C., Cook, B. D., Cook, D.,
1400 Coursolle, C., Cremonese, E., Curtis, P. S., D'Andrea, E., da Rocha, H., Dai, X.,
1401 Davis, K. J., Cinti, B., Grandcourt, A., Ligne, A., De Oliveira, R. C., Delpierre, N.,
1402 Desai, A. R., Di Bella, C. M., Tommasi, P. D., Dolman, H., Domingo, F., Dong, G.,
1403 Dore, S., Duce, P., Dufrene, E., Dunn, A., Dusek, J., Eamus, D., Eichelmann, U.,
1404 ElKhidir, H. A. M., Eugster, W., Ewenz, C. M., Ewers, B., Famulari, D., Fares, S.,
1405 Feigenwinter, I., Feitz, A., Fensholt, R., Filippa, G., Fischer, M., Frank, J., Galvagno,
1406 M., et al.: The FLUXNET2015 dataset and the ONEFlux processing pipeline for eddy
1407 covariance data, *Sci Data*, 7, 225, <https://doi.org/10.1038/s41597-020-0534-3>, 2020.

1408 Priestley, C. H. B. and TAYLOR, R. J.: On the assessment of surface heat flux and
1409 evaporation using large-scale parameters, *Monthly weather review*, 100, 81–92, 1972.

1410 Qi, W., Liu, J., and Chen, D.: Evaluations and Improvements of GLDAS2.0 and
1411 GLDAS2.1 Forcing Data's Applicability for Basin Scale Hydrological Simulations in
1412 the Tibetan Plateau, *JGR Atmospheres*, 123, <https://doi.org/10.1029/2018JD029116>,
1413 2018.

1414 Qi, W., Liu, J., Yang, H., Zhu, X., Tian, Y., Jiang, X., Huang, X., and Feng, L.: Large
1415 Uncertainties in Runoff Estimations of GLDAS Versions 2.0 and 2.1 in China, *Earth
1416 and Space Science*, 7, e2019EA000829, <https://doi.org/10.1029/2019EA000829>, 2020.

1417 Restrepo-Coupe, N., Albert, L. P., Longo, M., Baker, I., Levine, N. M., Mercado, L.
1418 M., da Araujo, A. C., Christoffersen, B. O., Costa, M. H., Fitzjarrald, D. R., Galbraith,
1419 D., Imbuzeiro, H., Malhi, Y., von Randow, C., Zeng, X., Moorcroft, P., and Saleska,
1420 S. R.: Understanding water and energy fluxes in the Amazonia: Lessons from an
1421 observation-model intercomparison, *Glob Chang Biol*, 27, 1802–1819,
1422 <https://doi.org/10.1111/gcb.15555>, 2021.

1423 Ribal, A. and Young, I. R.: Global Calibration and Error Estimation of Altimeter,
1424 Scatterometer, and Radiometer Wind Speed Using Triple Collocation, *Remote
1425 Sensing*, 12, <https://doi.org/10.3390/rs12121997>, 2020.

1426 Rodell, M., Houser, P., Jambor, U., Gottschalck, J., Mitchell, K., Meng, C.-J.,
1427 Arsenault, K., Cosgrove, B., Radakovich, J., and Bosilovich, M.: The global land data
1428 assimilation system, *Bulletin of the American Meteorological society*, 85, 381–394,

1429 2004.

1430 Sheffield, J., Goteti, G., and Wood, E. F.: Development of a 50-Year High-Resolution
 1431 Global Dataset of Meteorological Forcings for Land Surface Modeling, *Journal of*
 1432 *Climate*, 19, 3088–3111, <https://doi.org/10.1175/JCLI3790.1>, 2006.

1433 Stoffelen, A.: Toward the true near-surface wind speed: Error modeling and
 1434 calibration using triple collocation, *Journal of Geophysical Research: Oceans*, 103,
 1435 7755–7766, <https://doi.org/10.1029/97jc03180>, 1998.

1436 Su, C.-H. and Ryu, D.: Multi-scale analysis of bias correction of soil moisture,
 1437 *Hydrology and Earth System Sciences*, 19, 17–31, 2015.

1438 Su, C.-H., Ryu, D., Crow, W. T., and Western, A. W.: Beyond triple collocation:
 1439 Applications to soil moisture monitoring, *Journal of Geophysical Research:*
 1440 *Atmospheres*, 119, 6419–6439, <https://doi.org/10.1002/2013jd021043>, 2014.

1441 Sun, J., McColl, K. A., Wang, Y., Rigden, A. J., Lu, H., Yang, K., Li, Y., and
 1442 Santanello, J. A.: Global evaluation of terrestrial near-surface air temperature and
 1443 specific humidity retrievals from the Atmospheric Infrared Sounder (AIRS), *Remote*
 1444 *Sensing of Environment*, 252, <https://doi.org/10.1016/j.rse.2020.112146>, 2021.

1445 Towner, J., Cloke, H. L., Zsoter, E., Flamig, Z., Hoch, J. M., Bazo, J., Coughlan de
 1446 Perez, E., and Stephens, E. M.: Assessing the performance of global hydrological
 1447 models for capturing peak river flows in the Amazon basin, *Hydrology and Earth*
 1448 *System Sciences*, 23, 3057–3080, <https://doi.org/10.5194/hess-23-3057-2019>, 2019.

1449 Tsamalis, C.: Clarifications on the equations and the sample number in triple
 1450 collocation analysis using SST observations, *Remote Sensing of Environment*, 272,
 1451 <https://doi.org/10.1016/j.rse.2022.112936>, 2022.

1452 Twine, T. E., Kustas, W., Norman, J., Cook, D., Houser, Pr., Meyers, T., Prueger, J.,
 1453 Starks, P., and Wesely, M.: Correcting eddy-covariance flux underestimates over a
 1454 grassland, *Agricultural and forest meteorology*, 103, 279–300, 2000.

1455 Vogelzang, J., Stoffelen, A., and Verhoef, A.: The Effect of Error Non-Orthogonality
 1456 on Triple Collocation Analyses, *Remote Sensing*, 14, 4268, 2022.

1457 Wu, K., Ryu, D., Nie, L., and Shu, H.: Time-variant error characterization of SMAP
 1458 and ASCAT soil moisture using Triple Collocation Analysis, *Remote Sensing of*
 1459 *Environment*, 256, <https://doi.org/10.1016/j.rse.2021.112324>, 2021.

1460 Yang, Y., Roderick, M. L., Guo, H., Miralles, D. G., Zhang, L., Fatichi, S., Luo, X.,
 1461 Zhang, Y., McVicar, T. R., Tu, Z., Keenan, T. F., Fisher, J. B., Gan, R., Zhang, X.,
 1462 Piao, S., Zhang, B., and Yang, D.: Evapotranspiration on a greening Earth, *Nat Rev*

1463 Earth Environ, <https://doi.org/10.1038/s43017-023-00464-3>, 2023.

1464 Yilmaz, M. T. and Crow, W. T.: The optimality of potential rescaling approaches in
1465 land data assimilation, *Journal of Hydrometeorology*, 14, 650–660, 2013.

1466 Yilmaz, M. T. and Crow, W. T.: Evaluation of Assumptions in Soil Moisture Triple
1467 Collocation Analysis, *Journal of Hydrometeorology*, 15, 1293–1302,
1468 <https://doi.org/10.1175/JHM-D-13-0158.1>, 2014.

1469 Yilmaz, M. T., Crow, W. T., Anderson, M. C., and Hain, C.: An objective
1470 methodology for merging satellite- and model-based soil moisture products, *Water
1471 Resources Research*, 48, n/a-n/a, <https://doi.org/10.1029/2011wr011682>, 2012.

1472 Yin, G. and Park, J.: The use of triple collocation approach to merge satellite- and
1473 model-based terrestrial water storage for flood potential analysis, *Journal of
1474 Hydrology*, 603, <https://doi.org/10.1016/j.jhydrol.2021.127197>, 2021.

1475 Yin, L., Tao, F., Chen, Y., Liu, F., and Hu, J.: Improving terrestrial evapotranspiration
1476 estimation across China during 2000–2018 with machine learning methods, *Journal of
1477 Hydrology*, 600, <https://doi.org/10.1016/j.jhydrol.2021.126538>, 2021.

1478 Zhang, Y., Leuning, R., Hutley, L. B., Beringer, J., McHugh, I., and Walker, J. P.:
1479 Using long-term water balances to parameterize surface conductances and calculate
1480 evaporation at 0.05 spatial resolution, *Water Resources Research*, 46, 2010.

1481 Zhang, Y., Kong, D., Gan, R., Chiew, F. H. S., McVicar, T. R., Zhang, Q., and Yang,
1482 Y.: Coupled estimation of 500 m and 8-day resolution global evapotranspiration and
1483 gross primary production in 2002–2017, *Remote Sensing of Environment*, 222, 165–
1484 182, <https://doi.org/10.1016/j.rse.2018.12.031>, 2019.

1485 Zhao, M., Liu, Y., and Konings, A. G.: Evapotranspiration frequently increases during
1486 droughts, *Nature Climate Change*, 1–7, 2022.

1487 Zhu, G., Li, X., Zhang, K., Ding, Z., Han, T., Ma, J., Huang, C., He, J., and Ma, T.:
1488 Multi-model ensemble prediction of terrestrial evapotranspiration across north China
1489 using Bayesian model averaging, *Hydrological Processes*, 30, 2861–2879,
1490 <https://doi.org/10.1002/hyp.10832>, 2016.

1491 Zwieback, S., Su, C.-H., Gruber, A., Dorigo, W. A., and Wagner, W.: The impact of
1492 quadratic nonlinear relations between soil moisture products on uncertainty estimates
1493 from triple collocation analysis and two quadratic extensions, *Journal of
1494 Hydrometeorology*, 17, 1725–1743, 2016.

1495